HHS Public Access

Author manuscript

Nat Immunol. Author manuscript; available in PMC 2020 December 22.

Published in final edited form as:

Nat Immunol. 2020 July ; 21(7): 777–789. doi:10.1038/s41590-020-0706-5.

Bcl-6 is the nexus transcription factor of T follicular helper cells (T_{FH}) via repressor-of-repressor circuits

Jinyong Choi[1], **Huitian Diao**[2], **Caterina E. Faliti**[1], **Jacquelyn Truong**[1], **Meghan Rossi**[1], **Simon Bélanger**[1], **Bingfei Yu**[3], **Ananda W. Goldrath**[3], **Matthew E. Pipkin**[2], **Shane Crotty**[1,4,5,*]

[1]Center for Infectious Disease and Vaccine Research, La Jolla Institute for Immunology (LJI), La Jolla, CA, USA

[2]Department of Immunology and Microbiology, The Scripps Research Institute, Jupiter, FL, USA

[3]Division of Biological Sciences, University of California, San Diego, La Jolla, CA, USA

[4]Department of Medicine, Division of Infectious Diseases and Global Public Health, University of California, San Diego (UCSD), La Jolla, CA, USA

[5]Lead contact

Abstract

T follicular helper (T_{FH}) cells are a distinct type of $CD4^+$ T cells that are essential for most antibody and B lymphocyte responses. T_{FH} cell regulation and dysregulation is involved in a range of diseases. Bcl-6 is the lineage defining transcription factor of T_{FH} cells and its activity is essential for T_{FH} cell differentiation and function. However, how Bcl-6 controls T_{FH} biology has largely remained unclear, at least in part due to intrinsic challenges of connecting repressors to gene upregulation in complex cell types with multiple possible differentiation fates. Multiple competing models were tested here by a series of experimental approaches to determine that Bcl-6 exhibited negative autoregulation and controlled pleiotropic attributes of T_{FH} differentiation and function, including migration, costimulation, inhibitory receptors, and cytokines, via multiple repressor-of-repressor gene circuits.

*Correspondence: shane@lji.org (S.C.).

AUTHOR CONTRIBUTIONS

J.C. designed and performed experiments, analyzed the data, and wrote the manuscript. H.D. and M.E.P analyzed ATAC-seq data. C.E.F. developed CRISPR/Cas9-mediated gene deletion experiments. J. T., M. R., and S.B. performed experiments. B.Y. performed PageRank analysis. A.W.G and M.E.P provided advice, reagents, and computational analyses. S.C. supervised the project, designed experiments, analyzed data, and wrote the manuscript.

Reporting Summary. Further information on research design is available in the Nature Research Reporting Summary linked to this article.

DATA AVAILABILITY

RNA-seq and ATAC-seq data are deposited to the the Gene Expression Omnibus (GEO) under the GSE140187 super series (https://www.ncbi.nlm.nih.gov/geo/query/acc.cgi?acc=GSE140187). Scripts for analysis are deposited on Github: https://github.com/ScrippsPipkinLab/JYC_DataAnalysis. All other data that support the findings of this study are available from the corresponding author upon request.

COMPETING INTERESTS

The authors have no competing interests to declare.

INTRODUCTION

The formation of germinal centers (GCs) is essential for the development of high-affinity memory B cells and antibody secreting long-lived plasma cells in response to pathogen infections or vaccinations[1]. Follicular helper T cells (T_{FH}) provide key signals to antigen-specific B cells for the development of germinal center B (B_{GC}) cells[1,2]. $CD4^+$ T cells receiving T_{FH} inductive signals upregulate Bcl-6, the lineage defining transcription factor (TF) of T_{FH} cells[3–5]. Upregulation of Bcl-6 is associated with expression of the chemokine receptor CXCR5 and reduction of CCR7 and PSGL1, among other molecules, allowing for migration to the T-B border and GCs[1], the sites where T_{FH} and then GC-T_{FH} cells interact with antigen-specific B cells. T_{FH} and GC-T_{FH} cells express many surface and secreted molecules that serve as positive markers and contribute to the differentiation (ICOS, IL-6Rα, PD-1), migration (CXCR5, CD69), and function (IL-21, IL-4, CXCL13, SAP, ICOS, PD-1, CD200, CD40L) of T_{FH} and GC-T_{FH} cells. GC-T_{FH} cells provide IL-21, IL-4, and CD40L that are required for B_{GC} cell survival, proliferation, and somatic hypermutation[1,2,6].

Bcl-6 function is critical in T_{FH} differentiation[3–5]. Multiple TFs in addition to Bcl-6 have been identified that regulate T_{FH} differentiation[2,7–18]. Inhibition of Blimp-1 (encoded by *Prdm1*) by Bcl-6 is required for T_{FH} differentiation[3]. Tcf-1 and Lef-1 are involved in early induction of Bcl-6 and repression of Blimp-1[19–21]. Downregulation of Id2 is important for CXCR5 expression by releasing E protein TFs such as E2A and Ascl2[22,23]. While the importance of Bcl-6 in T_{FH} cell development is clear, it is still unclear how Bcl-6 controls T_{FH} cell biology. Two studies using Bcl-6 ChIP-seq in human GC-T_{FH} cells and murine T_{FH} cells provided insights into Bcl-6–bound genes[24,25], but functional roles have remained largely untested, and there is no consensus on a mechanistic model of how Bcl-6 regulates T_{FH} cell biology. Bcl-6 and Blimp-1 are reciprocal antagonistic regulators of each other's genetic loci[3]. That interaction provides a powerful mechanism for a genetic switch in cell differentiation, as co-expression of Bcl-6 and Blimp-1 is a metastable state[26]. However, from an experimentalist perspective, their mutual antagonism confounds experimental designs to probe Bcl-6 (and Blimp-1) functions in $CD4^+$ T cells. Additionally, the putative nature of Bcl-6 as a repressor in $CD4^+$ T cells adds an extra layer of complexity for understanding gene regulation, as many signature T_{FH} genes are upregulated in the presence of Bcl-6. In the present study, we took a first principles based approach to defining and testing hypothetical models of how Bcl-6 may control T_{FH} biology.

RESULTS

T_{FH} differentiation is not a default pathway

One proposed model of T_{FH} differentiation is that T_{FH} differentiation is the default pathway for naive $CD4^+$ T cells activated by antigen presenting cells. In this model, the primary role of Bcl-6 would be to inhibit Blimp-1 to allow activated $CD4^+$ T cells to undergo a default T_{FH} differentiation pathway[27] (Extended Data Fig.1a–b). We tested this model by utilizing *Bcl6*$^{f/f}$*Prdm1*$^{f/f}$*Cre*^{CD4} mice. If T_{FH} differentiation is a default setting in activated $CD4^+$ T cells, then when Blimp-1 is absent Bcl-6 would not be required. *Bcl6*$^{f/f}$*Prdm1*$^{f/f}$*Cre*^{CD4} $CD45.1^+$ SMARTA cells were transferred into C57BL/6 mice, as were wild-type (WT),

Bcl6$^{f/f}$*Cre*^{CD4}, or *Prdm1*$^{f/f}$*Cre*^{CD4} SMARTA cells. Host mice were immunized with KLH-gp$_{61}$ in alum + cGAMP adjuvant (Fig.1a and Extended Data Fig.1c–d). Wild-type SMARTA cells differentiated into non-T$_{FH}$ (CXCR5^{lo}SLAM^{hi}), T$_{FH}$ (CXCR5^{+}SLAM^{lo} or CXCR5^{+}PSGL1$^{int/lo}$), and GC-T$_{FH}$ cells (CXCR5^{hi}PSGL1^{lo} or CXCR5^{hi}PD-1^{hi}) after KLH-gp$_{61}$ immunization (Fig.1b). *Prdm1*$^{f/f}$*Cre*^{CD4} SMARTA cells predominantly differentiated into T$_{FH}$ and GC-T$_{FH}$ cells. *Bcl6*$^{f/f}$*Cre*^{CD4} CD4^{+} T cells did not differentiate into T$_{FH}$ cells[3,28]. Notably, *Bcl6*$^{f/f}$*Prdm1*$^{f/f}$*Cre*^{CD4} CD4^{+} T cells failed to differentiate into T$_{FH}$ and GC-T$_{FH}$ cells. Similar results were observed in the context of an acute viral infection (see Supplementary Note; Extended Data Fig.1e–g). Adoptive transfer of *Bcl6*$^{f/f}$*Prdm1*$^{f/f}$*Cre*^{CD4} SMARTA cells demonstrated that the T$_{FH}$ differentiation defect was antigen-specific and CD4^{+} T cell-intrinsic[29]. Signature T$_{FH}$ surface markers were examined to determine whether *Bcl6*$^{f/f}$*Prdm1*$^{f/f}$*Cre*^{CD4} CD4^{+} T cells became *bona fide* T$_{FH}$ cells in response to acute LCMV infection. Expression of T$_{FH}$ signature surface proteins was dysregulated (Fig.1c), indicating that Bcl-6 has important functions in gene regulation beyond repression of Blimp-1 that are necessary for T$_{FH}$ differentiation in both immunization and viral infection contexts.

To assess the migration and function of *Bcl6*$^{f/f}$*Prdm1*$^{f/f}$*Cre*^{CD4} SMARTA cells, we transferred SMARTA cells into *Bcl6*$^{f/f}$*Cre*^{CD4} mice, followed by infection of the host mice with LCMV$_{Arm}$ (Fig.1d). *Bcl6*$^{f/f}$*Cre*^{CD4} mice were used as recipient mice to eliminate endogenous T$_{FH}$ help to B cells. *Bcl6*$^{f/f}$*Cre*^{CD4} mice receiving *Bcl6*$^{f/f}$*Cre*^{CD4} SMARTA cells did not generate B$_{GC}$ cells (FAS^{+}PNA^{+}) in response to LCMV$_{Arm}$ infection. Notably, mice receiving *Bcl6*$^{f/f}$*Prdm1*$^{f/f}$*Cre*^{CD4} SMARTA cells failed to generate B$_{GC}$ cells, in contrast to mice receiving wild-type or *Prdm1*$^{f/f}$*Cre*^{CD4} SMARTA cells (Fig.1e). Similarly, B$_{GC}$ and plasma cell (B$_{PC}$; IgD^{lo}CD138^{hi}) responses were negligible in mice receiving either *Bcl6*$^{f/f}$*Prdm1*$^{f/f}$*Cre*^{CD4} or *Bcl6*$^{f/f}$*Cre*^{CD4} SMARTA cells in response to KLH-gp$_{61}$ immunization (Fig.1d,f). ~50% of wild-type SMARTA cells migrated into B cell follicles and GCs (Fig.1g–h and Extended Data Fig.1h–i). *Bcl6*$^{f/f}$*Cre*^{CD4} SMARTA cells were mostly excluded from the B cell follicle[3]. *Bcl6*$^{f/f}$*Prdm1*$^{f/f}$*Cre*^{CD4} SMARTA cells did not generate any histologically observable GCs and exhibited a migration pattern indistinguishable from *Bcl6*$^{f/f}$*Cre*^{CD4} SMARTA cells. IgG titers were significantly decreased in mice receiving *Bcl6*$^{f/f}$*Prdm1*$^{f/f}$*Cre*^{CD4} or *Bcl6*$^{f/f}$*Cre*^{CD4} SMARTA cells (Fig.1i). Altogether, we conclude that differentiation into T$_{FH}$ cells is not the default pathway of activated CD4^{+} T cells, and Bcl-6 has important activities beyond inhibition of *Prdm1* for instructing functional GC-T$_{FH}$ and GC development.

Bcl-6 is an autoregulatory repressor in CD4^{+} T cells

In B cells, Bcl-6 is generally considered an obligate repressor of transcription, but Bcl-6 mechanisms of action have been controversial in CD4^{+} T cells. While Bcl-6 expression positively correlates with expression of many genes in T$_{FH}$ cells, including genes with Bcl-6 binding sites[24,25], a mechanistic connection between Bcl-6 binding and gene regulation has been lacking. One example target gene of interest is *Bcl6* itself. Bcl-6 binds to its own promoter in human and mouse GC-T$_{FH}$ cells[24,25]. This Bcl-6 binding site (*Bcl6* Promoter Site 1; BPS1) sequence is conserved among mammals (Extended Data Fig.2a). Given that Bcl-6 expression positively correlates with T$_{FH}$ differentiation, Bcl-6 has been considered a

plausible candidate for positive regulation by Bcl-6. In contrast, there is evidence in B cell tumor lines that BCL-6 exhibits negative autoregulation[30]. To test whether Bcl-6 acts as a repressor or an activator of its own expression in $CD4^+$ T cells, we first utilized a self-inactivating (SIN) retroviral vector (RV) to measure *Bcl6* promoter activity (Fig.2a and Extended Data Fig.2b). SMARTA cells were transduced with the wild-type Thy1.1-RV (an RV construct containing the proximal *Bcl6* promoter upstream of a Thy1.1 reporter) or ΔBPS1 Thy1.1-RV (a mutated *Bcl6* promoter construct with an 8-nt deletion mutation), transferred to recipient mice, and *Bcl6* promoter activity was analyzed in T_{FH} and T_H1 cells after acute LCMV infection (Extended Data Fig.2c–d). Wild-type *Bcl6* promoter activity (Thy1.1 expression) was reduced in T_{FH} cells compared to T_H1 cells. ΔBPS1 *Bcl6* promoter activity was increased in T_{FH} cells in comparison to the wild-type *Bcl6* promoter (Fig.2b). Thus, Bcl-6 appears to repress *Bcl6* promoter activity in T_{FH} cells by binding of Bcl-6 to the BPS1 locus.

To test whether Bcl-6 binding to the endogenous *Bcl6* promoter affects Bcl-6 expression *in vivo*, we generated a new CRISPR mouse line possessing the 8-nt ΔBPS1 mutation. ΔBPS1 or littermate control (WT) SMARTA cells were transferred into C57BL/6 mice and then host mice were infected with $LCMV_{Arm}$ (Extended Data Fig.2e–f). ΔBPS1 SMARTA cells had highly increased Bcl-6 expression only in T_{FH} cells, not in T_H1 cells, indicating that BPS1 acts as a cis-regulatory element of *Bcl6* expression only when cells express elevated Bcl-6. Deletion of BPS1 increased the frequency of T_{FH} cells ($CXCR5^{hi}SLAM^{lo}$) and GC-T_{FH} cells ($CXCR5^{hi}PSGL1^{lo}$ or $CXCR5^{hi}$Bcl-6^{hi}; Fig.2c–d). Changes in T_{FH}-associated proteins were observed specifically in T_{FH} cells (see Supplementary Note; Extended Data Fig.2g).

Ncor1 is a Bcl-6 corepressor[31]. BCL-6 binding at the *BCL6* promoter locus overlapped with NCOR binding in a human B cell line (Extended Data Fig.2h). To determine whether the Bcl-6 autoregulation in $CD4^+$ T cells involved Ncor1, we transferred SMARTA cells expressing an shRNAmir targeting *Ncor1* (sh*Ncor1*-RV) or a negative control sh*Cd8* into B6 mice followed by an acute $LCMV_{Arm}$ infection. sh*Ncor1*$^+$ SMARTA cells exhibited enhanced GC-T_{FH} cell development and Bcl-6 expression (Fig.2e). In sum, these data indicate that Bcl-6 represses its own expression in $CD4^+$ T cells, mediated in conjunction with co-repressor Ncor1, in a negative autoregulatory feedback loop at the *Bcl6* promoter, dampening T_{FH} and GC-T_{FH} cell accumulation.

Simple circuitry repressor-of-repressors model of Bcl-6

The findings above excluded the simplest model of Bcl-6 regulation of T_{FH} differentiation. A logical model for how Bcl-6 functions as the lineage defining TF of T_{FH} biology is that Bcl-6 instructs positive T_{FH} gene expression by a repressor-of-repressors mechanism. A simple circuitry model can be proposed (Fig.3a) wherein Bcl-6 inhibits a set of repressor TFs (“Bcl6-r” TFs, directly inhibited by Bcl-6) that in turn repress genes positively associated with T_{FH} biology (“Bcl6-rr” genes, genes inhibited by repressor TFs targeted by Bcl-6). Alternative cell fates (i.e., non-T_{FH} or $T_H1/T_H2/T_H17/iT_{REG}$) and genes downregulated as part of T_{FH} cell migration or function (e.g., *Selplg*, encoding PSGL1) may be downregulated by Bcl-6 directly in this simple gene circuitry model. Testing this model is difficult because of the mutually antagonistic relationship of Bcl-6 and Blimp-1. We

reasoned that $CD4^+$ T cells deficient in both Bcl-6 and Blimp-1 would be needed to gain insights into TFs directly regulated by Bcl-6.

To identify the putative set of Bcl6-r TFs, we conducted RNA-seq gene expression profiling of *Bcl6*$^{f/f}$*Prdm1*$^{f/f}$*Cre*^{CD4}, *Bcl6*$^{f/f}$*Cre*^{CD4}, *Prdm1*$^{f/f}$*Cre*^{CD4}, and wild-type SMARTA T_{FH} and T_H1 cells generated in response to acute $LCMV_{Arm}$ infection or KLH-gp_{61} immunization (Fig.3b and Extended Data Fig.3a). As a first analysis the effect of *Bcl6*/*Prdm1* double-deficiency on the T_{FH} biology, we assessed expression of a broad curated set[19,22,25] of T_{FH}-associated genes across all samples from RNA-seq gene expression profiling. *Bcl6*$^{f/f}$*Prdm1*$^{f/f}$*Cre*^{CD4} T_{FH}-like cells lost expression of positively T_{FH}-associated genes in comparison to wild-type T_{FH} cells or *Prdm1*$^{f/f}$*Cre*^{CD4} T_{FH} cells. Conversely, *Bcl6*$^{f/f}$*Prdm1*$^{f/f}$*Cre*^{CD4} T_H1-like cells had a gene expression profile different from wild-type T_H1 or *Bcl6*$^{f/f}$*Cre*^{CD4} T_H1 cells (Extended Data Fig.3b). Principal component analysis provided similar findings (Extended Data Fig.3c), supporting the overall hypothesis that T_{FH} is not a default differentiation pathway of $CD4^+$ T cells and Bcl-6 has important activities beyond inhibition of *Prdm1*. We next characterized the effect of *Bcl6*/*Prdm1* double-deficiency on the expression of all T_{FH}- and T_H1-associated genes (Extended Data Fig.3b–c). *Bcl6*$^{f/f}$*Prdm1*$^{f/f}$*Cre*^{CD4} T_{FH}-like cells had reduced expression of ~88% of genes upregulated in wild-type T_{FH} cells (Fig.3c). These data indicate that the vast majority of genes upregulated in T_{FH} cells required Bcl-6 for proper induction. Furthermore, *Bcl6*$^{f/f}$*Prdm1*$^{f/f}$*Cre*^{CD4} T_{FH}-like cells had increased expression of ~90% of genes upregulated in wild-type T_H1 cells, suggesting that Bcl-6 was required to properly repress most T_H1-associated genes. Taken together, Bcl-6 is broadly important for both induction of T_{FH} genes and repression of non-T_{FH} genes, consistent with, and expanding upon, previous observations[3–5,24,29].

To identify genes likely to be directly repressed by Bcl-6, we analyzed patterns of gene expression changes between the six different T_{FH} and T_H1 populations and naive $CD4^+$ T cells. K-means analysis (K=10) and hierarchical clustering bioinformatic approaches both readily separated four distinct major gene expression patterns (Extended Data Fig. 3d–e). To obtain gene lists associated with those four major cluster patterns, MAP-DP clustering was performed (Fig.3d). We then attempted to apply our simple circuitry model of Bcl-6 function to the MAP-DP clustering outcomes. Given that the data sets also include modulation of Blimp-1 expression, and that Blimp-1 has major effects on T_H1 versus T_{FH} differentiation, we posited that a similar circuitry model of Blimp-1–mediated gene regulation may need to be included (Fig.3e). We therefore assessed whether the four major gene expression patterns regulated in T_{FH} and T_H1 cells could be largely accounted for by this simple circuitry model of Bcl-6 and Blimp-1 functioning as repressors. The model predicts that T_{FH} upregulated genes (Bcl6-rr) are upregulated via a Bcl-6 repressor-of-repressors mechanism (Fig.3e). If the model was accurate, these Bcl6-rr genes would correspond to Cluster 4, as expression of such genes would be reduced in *Bcl6*$^{f/f}$*Prdm1*$^{f/f}$*Cre*^{CD4} T_{FH}-like cells compared to *Prdm1*$^{f/f}$*Cre*^{CD4} T_{FH} cells (Fig.3d–e). Indeed, many genes upregulated in wild-type T_{FH} cells and important for the differentiation and function of T_{FH} cells were observed in Cluster 4, including *Cxcr5, Icos, Cd200, Pdcd1, Sh2d1a, Tcf7, Lef1, Tox, Tox2, Il6ra*, *IL4*, and *Il21*.

The model predicts that genes directly repressed by Bcl-6 (Bcl6-r) would fall into Cluster 1 (Fig.3e). Genes associated with alternative cell fates directly repressed by Bcl-6 would also group in Cluster 1. Important genes associated with non-T_{FH} fates do indeed group in Cluster 1[23] (Fig.3d). *Bcl6*$^{f/f}$*Prdm1*$^{f/f}$*Cre*^{CD4} T_{FH}-like cells had increased T_H1, T_H2, and T_{REG} signature genes expression (Fig.3f). Thus, multiple analytical approaches identified major gene networks and expression changes consistent with the proposed Bcl-6 repressor-of-repressors model.

If the Bcl-6 repressor-of-repressor model was accurate, a substantial proportion of Cluster 1 genes should represent genes directly repressed by Bcl-6 binding (Bcl6-r), while Cluster 4 genes should largely represent genes not directly bound by Bcl-6 (Bcl6-rr). To test this, we used the gene set of BCL-6-bound genes in human GC-T_{FH} cells identified by BCL-6 ChIP-Seq[24] and performed GSEA against Clusters 1 & 4 (see Supplementary Note). BCL-6–bound genes were highly enriched in Cluster 1 (Fig. 3g). In contrast, BCL-6-bound genes were not enriched in Cluster 4 (Fig.3g). Similarly, BCL-6-bound genes also were not enriched in Cluster 2 & 3 (Extended Data Fig.3f). Our model predicted that Cluster 2 & 3 would contain genes regulated by Blimp-1 (Blimp1-rr and Blimp1-r), with Cluster 3 genes directly targeted by Blimp-1 (Fig.3e). GSEA using Blimp-1-bound gene sets showed that Cluster 3 genes were highly enriched for Blimp-1-bound genes (Fig.3h and Extended Data Fig.3g), consistent with the model proposed. While the analyses do not exclude the possibility of some activity of Bcl-6 as an activator (see Supplementary Note), taken together, the data support the proposed model that Bcl-6 primarily acts as a repressor in regulating T_{FH} biology.

Bcl-6, Blimp-1, and Id2 relationships regulate *Cxcr5*

Among genes directly repressed by Bcl-6, TFs were of particular interest. Id2 was identified in the clustering analysis as a Bcl6-r TF (Fig.4a). We previously demonstrated that Id2 is an important regulator of T_{FH} differentiation[22]. Bcl-6 directly represses Id2, and Id2 inhibits CXCR5 expression via complexing with E proteins[22,23]. GSEA showed that E2A-bound genes were enriched in Cluster 4 (Fig.4b). Therefore, a minimalist T_{FH} differentiation model would be that Bcl-6 initiates and controls T_{FH} biology primarily via repression of two inhibitory TFs: Blimp-1 and Id2 (Fig.4c). To test the model, we generated *Bcl6*$^{f/f}$*Prdm1*$^{f/f}$*Id2*$^{f/f}$*Cre*^{CD4} SMARTA mice. *Bcl6*$^{f/f}$*Prdm1*$^{f/f}$*Id2*$^{f/f}$*Cre*^{CD4} CD4$^+$ T cells exhibited substantial increases in CXCR5 expression in comparison to *Bcl6*$^{f/f}$*Prdm1*$^{f/f}$*Cre*^{CD4} CD4$^+$ T cells (Fig.4d–e). However, GC-T_{FH} differentiation by *Bcl6*$^{f/f}$*Prdm1*$^{f/f}$*Id2*$^{f/f}$*Cre*^{CD4} CD4$^+$ T cells remained extremely defective (Fig.4f–g and Extended Data Fig. 4a–g). These data indicated that Bcl-6 likely represses multiple TFs in addition to Blimp-1 and Id2 to control T_{FH} biology.

Identification of Bcl-6 target TF candidates

Which TFs in addition to Blimp-1 and Id2 are key repressors downstream of Bcl-6 that control genes upregulated in T_{FH} cells? The simple circuitry repressor-of-repressors model predicts that such TFs should be present in Cluster 1 (Fig.3e). 307 TFs were identified in Cluster 1 (Fig.5a). We developed an analytical approach to identify candidate TFs by integrated analysis of the composite RNA-seq data with both BCL-6 ChIP-seq data from

human tonsillar GC-T_{FH} cells[24] and ATAC-seq of T_{FH} and non-T_{FH} cells from multiple genetically modified mice. Among the Cluster 1 TFs, 119 TFs represented BCL-6–bound gene loci in human GC-T_{FH} cells, confirming that these 119 TFs are direct targets of BCL-6 (Fig.5b).

The most functionally important Bcl6-r TFs would repress Bcl6-rr genes, based on the repressor-of-repressors Bcl-6 model (Fig.3a). We reasoned that candidate Bcl6-r TFs could be functionally connected to transcriptional regulation of genes upregulated in wild-type T_{FH} cells in a Bcl-6-dependent manner by testing for enrichment of candidate TF DNA binding motifs in differentially accessible chromatin regulatory regions of T_{FH}-associated genes, particularly between *Prdm1*$^{f/f}$ T_{FH} and *Bcl6*$^{f/f}$*Prdm1*$^{f/f}$ T_{FH}-like cells, as those chromatin changes would be dependent on Bcl-6 expression. We therefore conducted ATAC-seq of T_{FH} or T_H1 populations of *Bcl6*$^{f/f}$*Prdm1*$^{f/f}$*Cre*^{CD4}, *Bcl6*$^{f/f}$*Cre*^{CD4}, *Prdm1*$^{f/f}$*Cre*^{CD4}, and wild-type SMARTA cells in the context of acute $LCMV_{Arm}$ infection (Fig.5c). Several genes of interest were examined as a first test. An E2A binding motif was identified in a differential T_{FH} ATAC-seq peak in a downstream enhancer of *Cxcr5*, consistent with Bcl-6 control of CXCR5 expression via inhibition of Id2 (Extended Data Fig.5a–b). *Selplg*, *Tbx21*, and *Gata3* are known Bcl-6-bound genes[24]. Substantial changes in chromatin accessibility were observed for each of these genes. BCL-6 binding sites of these genes in human GC-T_{FH} cells were conserved in mouse by syntenic analysis (Fig.5d and Extended Data Fig.5c,d). A differential T_{FH} ATAC-seq peak in an *Selplg* intron overlapped with a large human GC-T_{FH} BCL-6 ChIP-Seq peak[24] centered on a BCL-6 DNA binding motif (*SELPLG* E1) (Fig.5d and Extended Data Fig.5d). To evaluate whether *SELPLG* E1 BCL-6 binding is conserved in mouse T_{FH}, we performed Bcl-6 ChIP with Myc-tagged Bcl-6 expressing (myctagN-*Bcl6*-RV$^+$) *Bcl6*$^{f/f}$*Cre*^{CD4} T_{FH} cells. Human BCL-6 bound *SELPLG* E1 in GC-T_{FH} was indeed a site bound by Bcl-6 in mouse T_{FH} cells (Fig.5e). Together, these results indicated the ATAC-seq data were high quality and could be used for broader TF motif scanning.

We then applied the differential chromatin accessibility plus TF motif analysis to all genes, across all ATAC-seq data sets, to identify TF motifs that were enriched within regions that underwent differential chromatin remodeling. Chromatin accessibility in the seven cell populations was distinct (Fig.6a). We scanned for 566 known TF-binding motifs within each differentially accessible ATAC peak in the genome. Motifs recognized by TFs Runx, Ets, T-box and Klf families were most highly enriched in chromatin regions with increased accessibility in *Bcl6*$^{f/f}$*Prdm1*$^{f/f}$ T_{FH}-like cells compared against *Prdm1*$^{f/f}$ T_{FH} cells (each $p<1.0 \times 10^{-16}$) and wild-type T_{FH} cells (Fig.6b). In contrast, in the same cell type comparisons, these TF motifs were depleted from chromatin regions with reduced accessibility (Extended Data Fig.6a). Changes in abundance of Runx DNA binding motifs were particularly significant ($p<9 \times 10^{-75}$). Runx and Tbet footprints were present (Fig.6c and Extended Data Fig.6b), indicating Bcl-6 expression prevents Runx and T-box family TFs from binding these sites, most likely by direct Bcl-6 transcriptional repression of Runx and T-box family genes. Runx DNA binding sites were observed in enhancer regions of T_{FH}-associated genes including *Pdcd1* and *Icos* (Fig.6d and Extended Data Fig.6c). All three Runx TFs are expressed in CD4$^+$ T cells (Fig.6e), and each Runx TF is known to be competent for binding consensus Runx motifs[32]. Runx2 and Runx3 were grouped in Cluster

1 in the gene expression MAP-DP clustering analysis (Fig. 3d), making them the more likely Runx candidates for repression by Bcl-6. BCL-6 bound robustly to *RUNX2* and *RUNX3*[24] enhancers in human GC-T_{FH} cells (Fig.6f). Bcl-6 bound *Runx2* E1, *Runx2* E2, *Runx2* E3, and *Runx3* E1 in mouse T_{FH} cells, confirming conservation of Bcl-6 binding to *Runx2* and *Runx3* loci (Fig.6g).

Enrichment of Klf DNA binding motifs in *Bcl6*$^{f/f}$*Prdm1*$^{f/f}$ T_{FH}-like cells was examined further. Several Klf-family TFs are expressed in CD4$^+$ T cells, with Klf2 representing the dominant member (Extended Data Fig.6d). Klf2 exhibited a Cluster 1 type gene expression pattern in T_{FH} cells in the context of KLH-gp_{61} immunization, while it exhibited a more complex gene expression pattern in acute LCMV infection (Fig.6h). The TF footprints for several Klf motifs were enriched in wild-type T_H1 cells over wild-type T_{FH} cells (Extended Data Fig.6b,e). Bcl-6 bound the *Klf2* promoter (P1) and a putative distal enhancer (DE), confirming that Bcl-6 binding sites at *Klf2* loci are conserved between humans and mice (Fig.6f,i). Klf binding sites were observed in open chromatin regions of multiple signature GC-T_{FH} genes (Fig.6d and Extended Data Fig.6c). These results identified Klf2 as a Bcl6-r TF candidate. GATA-3 is constitutively expressed in CD4$^+$ T cells. *Gata3* was defined as a Cluster 1 gene, with reduction of GATA-3 expression in T_{FH} cells compared to T_H1 cells (Fig.3d and Extended Data Fig.5c). Taken together, integrated bioinformatic analyses revealed Runx2, Runx3, GATA-3, and Klf2 as strong potential Bcl6-r TF candidates that repress T_{FH} genes.

Bcl-6 repressor-of-repressors circuits

To test the *in vivo* roles of candidate Bcl6-r TFs, we optimized a system for direct transfection of SMARTA cells with target gene CRISPR RNA (crRNA) and Cas9 ribonucleoprotein (RNP) complexes to disrupt target genes (Extended Data Fig.7a–b). RNP$^+$ SMARTA cells were adoptively transferred into host mice subsequently infected with $LCMV_{Arm}$. *Bcl6* and *Prdm1* were first tested as positive control genes (Fig.7a–b and Extended Data Fig.7c). crRNA-mediated deletion of TFs was efficient and was a suitable experimental system for exploring the genetics of T_{FH} biology *in vivo*. We then disrupted *Gata3*, *Runx2, Runx3,* and *Klf2* as candidate Bcl6-r T_{FH} repressors, with crRNA RNPs in *Bcl6*$^{f/f}$*Prdm1*$^{f/f}$*Cre*^{CD4} SMARTA cells, and examined their differentiation in the context of acute LCMV infection. cr*Cd8*$^+$ wild-type SMARTA cells were used as controls. cr*Gata3*$^+$*Bcl6*$^{f/f}$*Prdm1*$^{f/f}$*Cre*^{CD4} SMARTA cells exhibited increased CXCR5 and reduced PSGL1 expression in comparison to cr*Cd8*$^+$*Bcl6*$^{f/f}$*Prdm1*$^{f/f}$*Cre*^{CD4} SMARTA cells (Fig.7c and Extended Data Fig.7). These results suggest that GATA-3 is a Bcl6-r TF that is a repressor of CXCR5 and a positive regulator of PSGL1.

Roles of Runx family TFs in T_{FH} biology are largely unknown. We first examined the impact of *Runx2* disruption on T_{FH} gene regulation (Fig.7d–f and Extended Data Fig.7). We observed significantly greater frequencies of CXCR5$^+$ T_{FH}-like cells among cr*Runx2*$^+$*Bcl6*$^{f/f}$*Prdm1*$^{f/f}$*Cre*^{CD4} CD4$^+$ T cells compared to cr*Cd8*$^+$ control cells. Expression of ICOS and CD200 was upregulated in the absence of Runx2 (Fig.7e–f). *Runx3* disruption also increased the development of CXCR5$^+$ T_{FH}-like cells on the *Bcl6*$^{f/f}$*Prdm1*$^{f/f}$*Cre*^{CD4}

background, as well as expression of ICOS and CD200 (Fig.7g–h), paralleling the T_{FH} gene regulation observed by Runx2.

We next investigated whether Runx2 and Runx3 act predominantly upstream or downstream of Bcl-6 in T_{FH} differentiation. The proposed Bcl-6 repressor-of-repressors model predicted that Runx2 and Runx3 would act downstream of Bcl-6. To test this, we transduced wild-type SMARTA cells with RVs expressing GFP alone (GFP-RV$^+$), Runx3 (*Runx3*-RV$^+$), or Runx2 (*Runx2*-RV$^+$), transferred the cells into B6 mice, and analyzed T_{FH} differentiation 7 days after acute $LCMV_{Arm}$ infection (Extended Data Fig.8a). Enforced Runx2 expression resulted in reduced T_{FH} and GC-T_{FH} differentiation relative to control cells. Expression of ICOS and CD200 was also reduced in *Runx2*-RV$^+$ T_{FH} cells, consistent with the *Runx2* gene disruption data. Constitutive Runx3 expression caused more severe disruption of T_{FH} differentiation than did Runx2 (Fig.7i, Extended Data Fig.8). Most notably, Bcl-6 expression was not affected by enforced Runx2 or Runx3 expression, indicating that Bcl-6 is indeed upstream of *Runx2* and *Runx3* in T_{FH} cells (Fig.7j). Disruption of Runx2 expression results in a gain of T_{FH} gene expression similar to that of Runx3 gene disruption (Fig.7e–h), indicating that both *Runx2* and *Runx3* are relevant targets of Bcl-6 *in vivo* for T_{FH} development.

Klf2 has been connected to T_{FH} differentiation in both mice and humans, downstream of ICOS signaling[13,14]. Klf2 represses CXCR5 expression and Klf2 binds the *Prdm1* locus, but different models were proposed for how Klf2 influences T_{FH} differentiation[13,14]. Thus, we investigated the effect of Klf2 on T_{FH} gene expression using the crRNA RNP SMARTA system to test the model that Klf2 may act downstream of Bcl-6 as a Bcl6-r TF in a repressor-of-repressors circuit (Fig.8 and Extended Data Fig.9a–d). In the *Bcl6*$^{f/f}$*Prdm1*$^{f/f}$*Cre*^{CD4} background, expression of PD-1, ICOS, CD200, and IL-6Rα were all significantly upregulated in cr*Klf2*$^+$ CD4$^+$ T cells versus cr*Cd8*$^+$ (Fig.8a–c). More surprisingly, expression of the T_{FH} cytokine IL-21 was significantly increased (Fig.8d and Extended Data Fig.9b). Given that result, we examined expression of IL-4, the other major cytokine expressed by T_{FH} cells. IL-4 expression was substantially increased in antigen-stimulated cr*Klf2*$^+$ versus cr*Cd8*$^+$ CD4$^+$ T cells in KLH-gp_{61} immunization (Fig.8e and Extended Data Fig.9d). This occurred even though GATA-3 expression was not changed in the absence of Klf2[13,14]. Disruption of *Klf2* did not affect the expression of Maf, a TF known to have a role in *Il21* and *Il4* expression[33,34] (Fig.8f and Extended Data Fig.9c).

These observations indicated that Klf2 is a negative regulator of the expression of PD-1, ICOS, CD200, IL-6Rα, IL-21, and IL-4. The regulation of IL-6Rα and ICOS by Klf2 was reminiscent of the role of Tcf-1 (the product of *Tcf7*), but opposite[19–21]. Multiple Klf motifs were observed in open chromatin regions of the *Tcf7* gene locus in T_{FH} cells, suggesting that *Tcf7* may be a Klf2-targeted TF (Extended Data Fig.9e). Therefore, we examined Tcf-1 expression in cr*Klf2*$^+$ *Bcl6*$^{f/f}$*Prdm1*$^{f/f}$*Cre*^{CD4} SMARTA cells. Expression of Tcf-1 protein was substantially increased in the absence of Klf2 (Fig.8f and Extended Data Fig.9c). In mouse T_{FH} cells, Tcf-1 binding was observed at the promoter and enhancers of multiple GC-T_{FH} signature genes including *Pdcd1*, *Il6ra* (Extended Data Fig.9f), *Icos* and *Il21*, all of which are upregulated in cr*Klf2*$^+$ *Bcl6*$^{f/f}$*Prdm1*$^{f/f}$*Cre*^{CD4} SMARTA cells. These data support a *Bcl-6* −| *Klf2* −| *Tcf7* pathway for upregulation of T_{FH} genes (Fig.8g). Klf and Tcf-1

binding motifs were observed concomitantly in open chromatin of multiple Bcl6-rr genes including *Pdcd1*, *Cd200*, and *Il21* (Fig.6d and Extended Data Fig.6c,9g), suggesting that Klf2 represses Bcl6-rr genes through a combinatorial mechanism via direct binding and by repression of *Tcf7*. Taken together, we conclude that Bcl-6 is a nexus for control of positive T_{FH} gene expression by repression of multiple repressors (Fig.8g).

DISCUSSION

T_{FH} differentiation is a multistage, multifactorial process[1]. How Bcl-6, the lineage defining TF of T_{FH} cells, accomplishes control of T_{FH} differentiation and function has remained unclear, at least in part because of the complexity of the biology, the antagonistic relationship between Bcl-6 and Blimp-1, and intrinsic challenges of studying repressors. The present study advances our mechanistic understanding of how Bcl-6 controls T_{FH} differentiation and function. We resolved several obstacles through a series of logical approaches, integrating analyses of multiple data sources from multiple genotypes and genetically modified cells. Our observations excluded the two simplest models of Bcl-6 regulation of T_{FH} differentiation via repression of Blimp-1 alone or Blimp-1 and Id2. Bioinformatic analyses identified numerous candidate Bcl6-r TFs, and experiments demonstrated that Runx2, Runx3, GATA-3, and Klf2 are Bcl-6 target TFs that regulate T_{FH} differentiation and function. We conclude that Bcl-6 is a nexus for control of positive T_{FH} gene expression by repression of multiple repressors.

Bcl-6 is an obligate repressor in B cells[30,35,36]. We find that Bcl-6 regulates its own expression by a negative autoregulatory loop in T_{FH} cells. Based on these and other data, we proposed that Bcl-6 drives upregulation of canonical genes of T_{FH} differentiation and function via repressor-of-repressors mechanisms. In addition, Bcl-6 represses alternative, non-T_{FH}, cell fates. Bcl-6 clearly inhibits non-T_{FH} differentiation fates via inhibition of *Prdm1*[2,3,9]. BCL-6 can also block $T_H1/T_H2/T_H17$ differentiation by repression of lineage-defining TFs *TBX21, GATA3*, and *RORA*[4–6,24,37], as well as by repressing genes central to those cells types (e.g. *Il17a*, *Il17f*, *Ifng*, *Il2ra*, and *Ifngr1*[4,5,24]). In contrast, testing the repressor-of-repressors model of Bcl-6 function required identification of Bcl6-r TFs that repress positive features of T_{FH} biology, downstream of Bcl-6. Our analytical approach to identify candidate Bcl6-r repressor TFs integrated RNA-seq, ChIP-Seq, and ATAC-seq. Id2 is one Bcl6-r TF clearly important for regulation of *Cxcr5*. We further identified Runx2, Runx3, GATA-3, and Klf2 as Bcl6-r TFs that repress important T_{FH} genes including PD-1, ICOS, CD200, IL-6Rα, IL-21, and IL-4. These observations demonstrate there are multiple repressors downstream of Bcl-6 that control T_{FH} genes. While the results do not exclude additional TFs, or additional mechanisms of action including potential direct activator activity of Bcl-6 (see Supplementary Note), the overall structure of the repressor-of-repressors Bcl-6 gene regulatory network can explain why T_{FH} differentiation is fully dependent on Bcl-6. In the absence of Bcl-6 no TF appears to substitute.

One might consider whether Bcl-6 acting as an obligate repressor in $CD4^+$ T cells is a rare case for a lineage defining TF. Bcl-6 was, of course, originally identified as the master regulator of B_{GC} differentiation, and it has been well characterized as an obligate repressor in B cells[30,35,36], though efforts have predominantly focused on genes downregulated in

B_{GC} cells. Foxp3 is a second lineage-defining TF that mainly acts as a repressor[38]. RORγT appears to act substantially through repressor activity in T_H17 cells, in concert with Maf[39]. The primary actions of T-bet in $CD4^+$ T cells may also be predominantly repressive[40]. As such, it has been proposed that a general primary function of lineage defining TFs may be to limit, by direct repression or other mechanisms, the number of genes that are induced broadly by TCR and cytokine signaling[41]. Bcl-6 is a clear example of this direct repression model, but the work here adds to that by demonstrating how genes positively associated with a cell type can be upregulated downstream of a lineage-defining TF via repressor-of-repressor mechanisms. Our results thus establish an overall structure of T_{FH} differentiation and gene regulation in a parsimonious model of Bcl-6 serving as the apex of a repressor-of-repressors network. This may also provide future insights into the biology of dysregulated T_{FH} or T_{FH}-like cells present in a range of biomedically relevant diseases such as atherosclerosis and autoantibody-mediated autoimmune diseases[1].

METHODS

Mice.

C57BL/6J (B6) and *Cre*^{CD4} and $CD45.1^+$ mice were obtained from the Jackson Laboratory. Mouse strains described below were bred and housed in specific pathogen–free conditions in accordance with the Institutional Animal Care and Use Guidelines of the La Jolla Institute. SMARTA mice (T cell antigen receptor (TCR) transgenic for I-A^b-restricted lymphocytic choriomeningitis virus (LCMV) glycoprotein (gp) 66–77 peptide)[42], *Bcl6*$^{f/f}$[43], *Prdm1*$^{f/f}$[44], and $CD45.1^+$ congenic mice were on a full B6 background. *Bcl6*$^{f/f}$ or *Prdm1*$^{f/f}$ mice were crossed to the SMARTA, *Cre*^{CD4}, and $CD45.1^+$ strains to generate *Bcl6*$^{f/f}$*Cre*^{CD4} $CD45.1^+$ SMARTA and *Prdm1*$^{f/f}$*Cre*^{CD4} $CD45.1^+$ SMARTA mice. *Bcl6*$^{f/f}$*Prdm1*$^{f/f}$*Cre*^{CD4} $CD45.1^+$ SMARTA mice were generated by crossing *Bcl6*$^{f/f}$*Cre*^{CD4} $CD45.1^+$ SMARTA and *Prdm1*$^{f/f}$*Cre*^{CD4} $CD45.1^+$ SMARTA strains. Blimp-1-YFP[45] or ΔBPS1 (described below) mice were crossed to the $CD45.1^+$ SMARTA strain to generate Blimp-1-YFP $CD45.1^+$ SMARTA or ΔBPS1 $CD45.1^+$ SMARTA mice. Both male and female mice (6–15 weeks of age) were used throughout the study, with sex- and age-matched T cell donors and recipients. All animal experiments were performed under protocols approved by the Institutional Animal Use and Care Committees of the La Jolla Institute for Immunology.

Adoptive cell transfer, infection, and immunization.

Adoptive transfer of congenically marked cells ($CD45.1^+$) into recipient mice ($CD45.2^+$) was performed by intravenous injection via the retroorbital sinus. For LCMV Armstrong ($LCMV_{Arm}$) infection, 10×10^3 naïve, transduced RV^+, or $crRNA^+$ $CD4^+$ T cells were transferred into each mouse. Recipient mice were injected intraperitoneally with 2.0×10^5 plaque-forming units (pfu) of $LCMV_{Arm}$ in plain DMEM. For protein immunization, 50×10^3 naïve or $crRNA^+$ $CD4^+$ T cells were transferred into each mouse. A total of 10 μg of keyhole limpet hemocyanin (KLH) conjugated with LCMV gp61–80 peptide ($KLH\text{-}gp_{61}$) was prepared in alum (Alhydrogel) only, alum + LPS (1 μg), alum + Poly (I:C) (10 μg), or alum + cyclic [G(3′,5′)pA(3′,5′)p] (3′,3′-cGAMP; 10 μg, Invivogen) adjuvants in a total volume of 20 μL and injected into each footpad of recipient mice. Alum + 3′,3′-cGAMP was chosen as the adjuvant combination because alum alone is a poor inducer of Blimp-1

(Extended Data Fig.1a). Transferred cells were allowed to rest in host mice for 1d (naive cells) or 3–4 d (RV^+ or $crRNA^+$ cells) before infection or immunization.

Plasmids and retroviral transduction.

pMIG (contains an IRES-GFP), pMIG-Bcl6, pMIG-Runx2myc, pMIG-Runx3myc retroviral (RV) plasmids, and pQCXIP (contains Thy1.1 and pGK-GFP) self-inactivating (SIN) RV plasmid were described previously[28,46,47]. pMIG-myctagN-Bcl6 plasmid was generated by insertion of sequences encoding the Myc-tag to those encoding the N-terminus of Bcl-6 with short-linker sequences (5′-GATCTGAATTCGGAATCTACC-3′). pQCXIP plasmid was further modified with deletion of the IRES-$Puro^R$ cassette and the CCAAT box and the TATA box of 3′-UTR to reduce background reporter expression (pQdT, Extended Data Fig. 2b). Constructs containing either wild-type or an 8-nt deletion that removes the Bcl-6 binding motif (+18; TCTAGGAA) in the proximal *Bcl6* promoter region (−709 to +272 from transcription start site) were cloned into the pQdT plasmid at the upstream of the Thy1.1 reporter to generate wild-type Thy1.1-RV or ΔBPS1 Thy1.1-RV, respectively (Fig.2a). Virions were produced by transfection of the Plat-E cell line. Culture supernatants were collected 24 and 48 h after transfection, filtered through a 0.45 μm syringe filter and stored at 4 °C until transduction. $CD4^+$ T cells were isolated from whole splenocytes by negative selection (Stemcell Technologies) and resuspended in R10 (RPMI1640 + 10% FBS, supplemented with 2 mM Glutamax, 100 U/ml Penicillin/Streptomycin, and non-essential amino acids (Gibco)) with 2 ng/ml recombinant human IL-7 (Peprotech) and 50 μM β-mercaptoethanol (2-ME). 0.5×10^6 cells were stimulated in 24-well plates pre-coated with 8 μg/ml anti-CD3 (17A2; BioXcell) and anti-CD28 (37.51; BioXcell). At 40 and 48 h after stimulation, cells were transduced by adding RV supernatants supplemented with 50 μM 2-ME and 8 μg/ml polybrene (Millipore), followed by centrifugation for 90 min at 524 x *g* at 37 °C. Following each transduction, the RV-containing medium was replaced with R10 + 50 μM 2-ME + 10 ng/ml human IL-2. After 72 h of *in vitro* stimulation, $CD4^+$ T cells were transferred into six-well plates in R10 + 50 μM 2-ME + 10 ng/ml human IL-2, followed by incubation for 2 days. One day before transfer, the culture medium was replaced with R10 + 50 μM 2-ME + 2 ng/ml human IL-7. Transduced cells were sorted based on GFP expression (FACSAria; BD Biosciences).

Enforced Runx3 (Runx3-RV^+ [High]) or Runx2 (Runx2-RV^+ [High]) expression disrupted T_{FH} differentiation relative to control cells (GFP-RV^+) (Extended Data Fig.8b,d). Since overexpression of Runx3 at much higher than the physiological level resulted in a negative effect on $CD4^+$ T cell accumulation (Extended Data Fig.8b,c), we made methodological improvements by performing similar experiments with lower constitutive Runx3 expression by sorting the bottom 10% GFP^+ cells (Runx3-RV^+ [Low]) instead of total GFP^+ SMARTA (Runx3-RV^+ [high]) for adoptive transfer (Extended Data Fig.8e–f). With lower enforced expression of Runx3, SMARTA cell proliferation was enhanced to levels similar to that of Runx2-RV^+ [Med] cells (Extended Data Fig.8g). Nevertheless, Runx3-RV^+ [Low] SMARTA still showed a stronger impaired T_{FH} and GC-T_{FH} development compared to Runx2-RV^+ [Med] SMARTA (Fig. 7i and Extended Data Fig.8h).

Generation of ΔBPS1 mice using CRISPR-Cas9 gene editing.

The *in vitro* molecular and cellular biology was performed by Ingenious Targeting Laboratory, Inc. Guide RNAs were selected using optimized CRISPR design by CHOP-CHOP (https://chopchop.cbu.uib.no/)[48]. Guide RNAs (gRNA1, 5′-caccgTCTAGGAAAGGCCGGACACC-3′ and 3′-cAGATCCTTTCCGGCCTGTGGcaaa-5′; gRNA2, 5′-caccgTGGTGATGCAAGAAGTTTCT-3′ and 3′-cACCACTACGTTCTTCAAAGAcaaa-5′) were cloned into px459-Cas9-puromycin plasmid. Lipofectamine transfection of each gRNA with a control gRNA was performed on Neuro2A cells (duplicate set per gRNA). The control gRNA was designed upstream of the gRNA. After 24 h, cells were selected for puromycin resistance for 3–5 days and then lysed. PCR analysis was performed to verify the cleavage efficiency of each gRNA. The cleavage efficiency of gRNA was 10–15%. An injection mix of 30 ng/μl Cas9 protein, 0.6 μM gRNA, and 20 ng/μl oligonucleotide (template DNA for the repair to delete the 8-nt Bcl-6 recognition motif) was injected into 150–250 fertilized eggs from C57BL/6J mice by the UCSD Stem Cell Core. These eggs were implanted into C57BL/6J surrogate mothers, and pups were genotyped by DNA sequencing. DNA sequences were analyzed and diagrammed using MacVector (Extended Data Fig.2e). ΔBPS1 mice were healthy, and immune cell development appeared grossly normal.

CRISPR/Cas9-mediated gene deletion of murine CD4$^+$ T cells.

High-ranked guide sequenes with the highest on-target and off-target scores were selected by CHOP-CHOP. crRNA and ATTO-550 conjugated tracrRNA were purchased from Integrated DNA Technologies, Inc. Purified *S. pyogenes* Cas9-NLS protein was purchased from QB3 Macrolab of University of California, Berkeley. crRNA and tracrRNA were duplexed by heating 95 °C for 5 min. Ribonucleoprotein (RNP) complexes were generated by mixing crRNA-tracrRNA duplexes (240 pmol) and Cas9-NLS protein (80 pmol) for 10 min at 24–26 °C. Isolated CD4$^+$ T cells were stimulated in 24-well plates pre-coated with 8 μg/ml anti-CD3 (17A2) and anti-CD28 (37.51) for 2 days. The cells were then transfected with a RNP mixture by electroporation using MaxCyte ATX with Expanded T cell-4 protocol (MaxCyte, Inc, MD). The transfected cells were cultured in R10 + 50 μM 2-ME + 10 ng/ml human IL-2 without TCR stimulation for 1 day, followed by culture for an additional day in R10 + 50 μM 2-ME + 2 ng/ml human IL-7. Transfection efficiency and cell viability were measured using LSRII or LSR Fortessa. RNP transfection efficiencies were consistently greater than 90%, with high viability (Extended Data Fig.7a,b). crRNA sequences used in the study: cr*Cd8*, 5′-GCAGGTTCAGCGACAGAAAG-3′; cr*Bcl6*, 5′-TCAAGATGTCCCGACTCCGG-3′; cr*Prdm1*, 5′-TTGGAACTAATGCCGTACGG-3′, cr*Runx2*, 5′-ACCATGGTGCGGTTGTCGTG-3′; cr*Runx3*, 5′-GCTAAGCGCGCAGGCAACCG-3′; cr*Gata3*, 5′- TGTACGAATGGCCGAGGCCC-3′; cr*Klf2*, 5′-CTGGCCGCGAAATGAACCCG-3′.

Wild-type or *Bcl6*$^{f/f}$*Prdm1*$^{f/f}$*Cre*^{CD4} SMARTA CD4$^+$ T cells transfected with cr*Cd8*, cr*Gata3*, cr*Runx2*, cr*Runx3*, or cr*Klf2* were transferred to C57BL/6 host mice, followed by infection with $LCMV_{Arm}$ or immunization with KLH-gp_{61} of the host mice, and analyzed 6–7 days later. SMARTA cells were sorted by flow cytometry from spleens or lymph nodes

of host mice. Gene knockdown efficiencies were measured by mRNA qPCR (for *Runx2* using a primer set: fwd, 5′- CACGACAACCGCACCAT-3′ and rev, 5′- CACGGAGCACAGGAAGTT-3′), flow cytometry (for Bcl-6 and GATA-3), or immunoblot analysis (Runx3 and Klf2). sh*Runx3*-RV$^+$ (gene knockdown) SMATRA cells and pMIG-Klf2-RV$^+$ (enforced expression) SMARTA cells were used as positive controls for immunoblot analysis.

Flow cytometry and cell sorting.

Single-cell suspensions of spleens or draining popliteal lymph nodes were prepared by standard gentle mechanical disruption. Surface staining for flow cytometry was done with monoclonal antibodies to CD4 (RM4–5), CD8 (53–6.7), SLAM (TC15–12F12.2), ICOS (C398.4A), CD200 (OX-90), CD138 (281–2) (from BioLegend), B220 (RA3–6B2), CD45.1 (A20), PD-1 (J43), CD44 (IM7) (from eBioscience), PSGL1 (2PH1), Fas (Jo2), IgD (11–26) (from BD Biosciences), PNA (FL-1071) (Vector Laboratories), and Fixable Viability Dye eFluor780 (eBioscience). Staining was performed for 30 min at 4 °C in PBS supplemented with 0.5% bovine serum albumin (BSA), unless specified otherwise. CXCR5 staining was done using biotinylated anti-CXCR5 (SPRCL5; eBioscience) for 30 min, followed by BV421 or PE.Cy7-labeled streptavidin (BioLegend) at 4 °C in PBS supplemented with 0.5% BSA. Intracellular staining for TFs was performed with monoclonal antibodies to Bcl-6 (K112–91, BD Biosciences), Tcf-1 (C63D9, Cell Signaling), T-bet (4B10), GATA-3 (TWAJ), Maf (Sym0F1) (from eBioscience) using the Foxp3/Transcription Factor Staining Buffer Set (eBioscience). For measurement of cytokines, the cells from spleen or lymph node were cultured *in vitro* for 5 h in 10 μg/ml $gp_{66–77}$ peptide (gp_{66}) and Brefeldin A. Intracellular staining for cytokines was performed with monoclonal antibody to IL-4 (11B11, eBioscience) and recombinant mouse IL-21 receptor Fc (R&D), followed by anti-human IgG (Invitrogen), using the Fixation/Permeabilization buffer kit (BD Biosciences). Stained cells were analyzed using LSRII, LSRFortessa, or FACS Celesta (BD) and FlowJo software v.10.6 (Flowjo, LLC). For cell sorting, CD45.1$^+$ SMARTA cells were pre-enriched with PE conjugated anti-mouse CD45.1 Ab (eBioscience) and anti-PE microbead (Miltenyi). All sorting was done on a FACSAria or FACSAria Fusion (BD Biosciences). Cellular data were presented as frequencies of cell populations; absolute numbers of cells were also determined. Frequency and absolute number conclusion were equivalent unless stated otherwise. Spleen and LN size were equivalent between samples unless stated otherwise.

ELISA.

Nunc MaxiSorp plates (Thermo Fisher Scientific) were coated overnight at 4 °C with 1 μg/ml KLH-gp_{61} (Genscript) in PBS. Plates were blocked with PBS + 0.05% Tween-20 + 0.5% BSA for 90 min at 25 °C. After washing, mouse serum was added in a serial dilution in PBS + 0.05% Tween-20 + 0.5% BSA (PBST-B) and incubated for 90 min. After washing, horseradish peroxidase (HRP)-conjugated goat anti-mouse IgG (Thermofisher Scientific) was added at 1:5,000 in PBST-B for 90 min at 25 °C. Colorimetric detection was performed using a TMB substrate kit (Thermofisher Scientific). Color development was stopped after approximately 5–10 min with 2 N H_2SO_4, and absorbance was measured at 450 nm.

Immunofluorescence staining of lymph node.

Popliteal lymph nodes from mice immunized with KLH-gp_{61} were snap frozen in OCT medium (Sakura Finetek, USA), and 5–8 μm sections were prepared using a cryostat. Lymph node sections were fixed with acetone-methanol, and stained with antibodies to TCRβ (BV421), IgD (AlexaFlour488), GL7 (PE), and CD45.1 (AlexaFlour647) to reveal the T cell zone, B cell zone, GCs, and SMARTA cells, respectively. Sections were fixed and mounted with ProLong gold antifade reagent (Invitrogen), and imaged by Zeiss AxioScan Z1 Slide Scanner. SMARTA cell localization was analyzed by ImageJ software (v2.0.0-rc-69/1.52p, NIH). The T-B border was defined as ±15 μm region at a boundary line between T cell zone and B cell zone (Extended Data Fig.1h).

RNA-seq.

RNA-seq was performed with a method previously described[49]. Spleens or LNs were isolated and pooled from 4–8 mice per group. 25,000–100,000 $CXCR5^+SLAM^{lo/int}$ T_{FH}, $CXCR5^{lo}SLAM^{hi}$ T_H1 SMARTA cells ($CD45.1^+CD4^+CD8^-B220^-$ singlets), or naïve SMARTA cells ($CD4^+CD8^-B220^-CD44^{lo}CD62L^{hi}$) were sorted using a FACSAria into Trizol LS (Invitrogen). RNA extraction was performed using miRNeasy micro kits (Qiagen) for downstream RNA-Smart-Seq2 input requirements[49]. cDNA was purified using AMPureXP beads (1:1 ratio; Beckman Coulter). One nanogram cDNA was used to prepare a standard Nextera XT sequencing library (Nextera XT DNA sample preparation and index kits; Illumina). Quality control steps were included to determine total RNA quality and quantity, the optimal number of PCR preamplification cycles, and fragment size selection. All samples passed the quality control. Libraries were sequenced using a HiSeq2500 to generate 50-bp single-end reads (TruSeq Rapid Kit; Illumina), generating median of >13 million ($LCMV_{Arm}$ infection) or >7 million (KLH-gp_{61} immunization) mapped reads per sample. Three ($LCMV_{Arm}$ infection) or 4 (KLH-gp_{61} immunization) biological replicates were generated.

RNA-seq analysis.

The single-end reads that passed Illumina filters were subsequently filtered for reads aligning to tRNA, rRNA, adapter sequences, and spike-in controls. The reads were aligned with the mm10 reference genome using TopHat (v1.4.1., library-type fr-secondstrand-C) and the RefSeq gene annotation downloaded from the University of California – Santa Cruz Genome Bioinformatics site. DUST scores were calculated with PRINSEQ Lite (v0.20.3) and low-complexity reads (DUST > 4) were removed from the BAM files. The alignment results were parsed via the SAMtools to generate SAM files. Read counts to each genomic feature were obtained with the HTSeq-count program (v0.7.1; -m union -s yes -t exon -i gene_id). After removing absent features (zero counts in all samples), the raw counts were imported to R/Bioconductor package DESeq2 (v3.1). *P*-values for differential expression were calculated using the Wald test and then adjusted for multiple test correction using Benjamini-Hochberg algorithm[50]. We considered genes differentially expressed between two groups of samples when the DESeq2 analysis resulted in an adjusted *P*-value of <0.05 and the difference in gene expression was 1.4-fold. Genes with raw counts less than 6 as minimum cutoff (an average raw count of *Cd8a* in all samples; *Cd8a* is considered to be not

expressed, or very weakly expressed in peripheral, splenic $CD4^+$ T cells.) were excluded from differential expression analysis. TPMs were calculated from raw count data by dividing by the number of counts by exon length in kilobases (RPK), dividing the total number of counts by 1 million (CM) and then dividing the RPK by CM. Principal Component Analysis (PCA) was performed using the 'prcomp' function in R.

We firstly assessed expression of a broad curated set[19,22,25] of T_{FH}-associated genes across all samples from RNA-seq gene expression profiling. Sequential clustering analyses were performed to analyze the patterns of gene expression changes between the six different T_{FH} and T_H1 populations. K-means analyses were firstly performed using K=10 for overall gene expression change patterns by ExpressCluster v1.3 software from CBDM Laboratory in Harvard School of Medicine (https://cbdm.hms.harvard.edu/). Total DEG genes (Fc > 1.4; adj. *P*-val < 0.05; pre-filtered with minimum cutoff) were subjected to the K-means clustering. Four major clusters (n= ~300 or more genes) of gene expression change were apparent. To obtain gene lists associated with those 4 major cluster patterns of gene expression, *Maximum a-posteriori Dirichlet process mixtures* (MAP-DP) clustering was then performed with predefined cluster centers according to the result from K-means analysis by R-ClustMAPDP[51]. We chose MAP-DP instead of K-means clustering because MAP-DP analysis efficiently separates outliers from the data and is statistically rigorous[51]. We used the following criteria for the 4 major clusters: (1) wild-type T_{FH} and *Prdm1*$^{f/f}$ T_{FH} have lower expression than the other populations; (2) wild-type T_H1 and *Bcl6*$^{f/f}$ T_H1 have higher expression than the other populations; (3) wild-type T_H1 and *Bcl6*$^{f/f}$ T_H1 have lower expression than the other populations; (4) wild-type T_{FH} and *Prdm1*$^{f/f}$ T_{FH} have higher expression than the other populations (Fig. 3d). Total DEG genes (Fc > 1.4; adj. *P*-val < 0.05; pre-filtered with minimum cutoff) were subjected to the MAP-DP analysis, as was done for the K-means clustering.

Hierarchical clustering analysis was performed with the genes upregulated or downregulated in T_{FH} cells relative to their expression in T_H1 cells (Fig. 3c; 1.4-fold cut off, Adj. *P*-val <0.05) using hclust function from stats package in R and the heatmap was generated using heatmap.2 function from gplots package in R.

Gene Set Enrichment Analysis (GSEA) was run on gene lists pre-ranked by DESeq log *P*-value multiplied by the sign of the log-fold change[52] with GSEA v3.0 (Broad Institute, Inc.).

Bcl-6–bound, Blimp-1–bound, and T_{FH}, T_H1, T_H2, T_H17, and T_{REG} signature gene lists were collected from previous studies[19,22,24,25,53,54] and from Ingenuity Pathway Analysis database (Qiagen). E2A target-gene list was generated by Shaw et al.[22] using ChIP-seq results from thymocytes by E2A Bio-ChIP method in previously described[55]. In multiple GSEA (Fig.3f), the nominal *P*-values were corrected with Benjamini-Hochberg algorithm.

ATAC-seq.

ATAC-seq was performed with a modified method from previously described[56]. Spleens were isolated and pooled from 3–5 mice per group. 5×10^4 $CXCR5^+SLAM^{lo/int}$ T_{FH}, $CXCR5^{lo}SLAM^{hi}$ T_H1 SMARTA cells ($CD45.1^+CD4^+CD8^-B220^-$ singlets), or naive SMARTA cells ($CD4^+CD8^-B220^-CD44^{lo}CD62L^{hi}$) were sorted using a FACSAria. Cells

were pelleted and resuspended in 25 μl lysis buffer, and spun down. The nuclear pellet was resuspended into 25 μl transposition reaction mixture containing Tn5 transposase from Nextera DNA Sample Prep Kit (Illumina) and incubated at 37 °C for 30 min. Then the transposase-associated DNA was purified using MinElute Purification kit (Qiagen). To amplify the library, the DNA was amplified for twelve cycles using KAPA Real-Time Library amplification kit (KAPAbiosystems) with Nextera indexing primers. The total amplified DNA was purified using AmPureXP beads. The quantity and size of amplified DNA was examined by TapeStation to confirm that independent samples exhibited similar fragment distributions. The libraries were sequenced using Hiseq4000 with paired-end sequencing (Illumina). Replicates were generated from 3 independent experiments.

ATAC-seq analysis.

Fastq reads were aligned with the mm10 reference genome with Bowtie2 (-p 15 -m 1 -best -strata -X 2000 -S –fr –chunkmbs 1024). PCR duplicates were removed by SAMtools. Peaks were called with MACS2 (macs2 callpeak –t inputfile –f BED –g mm –n outputfile –nomodel −1 0.01 –keep-dup all –call-sumits -B). Bigwig files for ATAC-seq signal visualization on UCSC genome browser was generated by converting MACS2 output read pileup file into bigwig files with bedgraphtobigwig from UCSC tools. Peaks from all samples were merged to create a common reference peak set using Homer (mergePeaks -d 200). Peaks localized within 100 kb upstream of the transcription start site (TSS) and 100 kb downstream of the transcription end site (TES) were annotated to a gene[46]. hTseq-count was used to calculate Tn5 insertion site number in peaks[57]. Scikit-learn was used for t-SNE analysis of Tn5 count matrix to visualize sample similarity[58]. For differential analysis, DEseq2 was used to compare Tn5 insertion site numbers in peaks for each condition after filtering out low read peaks (count number <5 in all samples in comparison). The relative open / close regions were defined by using DEseq2 to compare the Tn5 insertion site number within ATAC-seq peaks among samples (DEseq2 raw *P*-val < 0.05). Motif enrichment was performed by Homer (findMotifsGenome.pl -size given -mis 3 -mask), with combination of Homer curated known motif set, motifs from MEME motif database, and JASPAR database. Frequencies of the enriched TF motifs were determined in regions of increased or decreased accessibility (DEseq2 raw *P*-val < 0.05). Significance for the differences of TF motif enrichment across comparisons was determined by Chi-squared tests. Family of transcription factors were characterized with information from tFclass database[59]. Transcription factor footprint analyses were performed with RGT-hint[60] using JASPAR database. JASPAR motifs are described by a position weight matrix (PWM) providing information on the frequency of usage of each nucleotide in the motifs derived from experimental data, such as ChIP-seq[61]. Although two related TFs (e.g., Runx2 and Runx3) can bind the identical consensus sequences, use of the PWMs in JASPAR allows for non-identical assignments if the data support differential PWMs. PageRank analysis was performed with Taiji as previously described method[56], as a separate bioinformatic algorithm based on differential gene expression and TF binding motifs, with compatible results with differential ATAC-seq analysis (Extended Data Fig.6f), although the nature of the PageRank algorithm is more effective for identifying activator TFs instead of repressors.

ChIP-seq analysis.

Raw sequencing reads for Blimp-1 (GSE75724, GSE79339)[53,54], Tcf-1 (GSE103387)[62], and BCL-6 and NCOR (GSE29282)[35] were downloaded from the SRA database. Reads were aligned to UCSC mm9 (Blimp-1), mm10 (Tcf-1), or hg19 (BCL-6 and NCOR) with Bowtie (v1.1.2) using options (-S–fr -p 3 -m 1 -k 1–best –strata) and peaks were called using MACS with default settings. The UCSC tracks and peak calls of BCL-6 ChIP-seq data of human tonsillar GC-T_{FH} (GSE59933) were from the data of the original paper[24]. Peaks were annotated based on the RefSeq database. Peaks localized ±2 kb of the TSS were defined as promoter peaks, peaks localized ±2 kb of the TES were defined as 3′ end peaks, and peaks >2 kb away from genes were defined as intergenic[24]. Syntenic analysis of human Bcl-6-binding sites in the mouse genome was performed using the Liftover tool of UCSC Browser with default settings (https://genome.ucsc.edu/cgi-bin/hgLiftOver). The human BCL-6 binding peaks firstly converted from hg18 to mm9, and then converted from mm9 to mm10 (7,673 peaks were successfully converted to mouse genome from the original human 8,523 peaks). Bcl-6-binding in mouse genome was evaluated by ChIP-qPCR for some genes of interest.

ChIP-qPCR.

To validate whether Bcl-6 binding in human GC-T_{FH} cell is conserved in mouse T_{FH} cell, Bcl-6 ChIP-qPCR of mouse T_{FH} cells was performed using tagged-Bcl6 RV transduction. We confirmed that Bcl-6 protein from pMIG-Bcl6 (*Bcl6*-RV) was expressed at levels similar to that of endogenous Bcl-6 in T_{FH} cells (Extended Data Fig.5e). We then validated that an N-terminal Myc-tagged Bcl-6 fusion protein (myctagN-*Bcl6*-RV) was functionally comparable with non-tagged *Bcl6*-RV (*Bcl6*-RV), based on tag-Bcl6-RV rescue of T_{FH} differentiation and function of $Bcl6^{f/f}Cre^{CD4}$ $CD4^+$ T cells in LCMV infected mice (Extended Data Fig.5e,f). To perform myctagN-Bcl6 ChIP-qPCR, $Bcl6^{f/f}Cre^{CD4}$ SMARTA cells transduced with myctagN-Bcl6-RV were transferred to C57BL/6 mice, followed by infection of the host mice with $LCMV_{Arm}$. Seven days later, spleens were isolated and pooled from 30 mice, and pre-enriched $CD45.1^+GFP^+$ SMARTA cells were further sorted to obtain $CXCR5^+SLAM^{lo}$ T_{FH} cells. 9×10^6 T_{FH} cells were fixed in 1% formaldehyde for 2.5 min and then quenched with 125 mM glycine for 5 min. Cells were lysed using truChIP Chromatin Shearing Kit and sonicated to generate < 500-bp fragments using E220 Focused-ultrasonicator (Covaris). Fragmented DNA was used as input control. Magnetic Dynabeads (45 μL) were washed with IP buffer (50 mM NaCl, 5 mM EDTA, 50 mM Tris pH8.0, and 0.1% NP-40) and then mixed with 7.5 μg anti-Myc tag or goat IgG (Abcam) antibodies in 300 μl IP buffer and rotated for 6 h at 4 °C. The sonicated lysates were diluted in IP buffer at 1:4 ratio and precleared with Dynabeads for 2 h at 4 °C. The precleared lysates were added to antibody-conjugated Dynabeads and incubated overnight at 4 °C. The beads were washed with IP buffer once, Wash Buffer I (150 mM NaCl, 0.5% sodium deoxycholate, 1% NP-40, 0.1% SDS, 1 mM EDTA, and 50 mM Tris pH8.0) twice, Wash Buffer II (500 mM NaCl, 0.5% sodium deoxycholate, 1% NP-40, 0.1% SDS, 1 mM EDTA, and 50 mM Tris pH8.0) twice, Wash Buffer III (250 mM LiCl, 0.5% sodium deoxycholate, 1% NP-40, 0.1% SDS, 1 mM EDTA, and 50 mM Tris pH8.0) twice, and TE buffer twice for 5 min each. The beads were resuspended in 200 μl Elution Buffer (100 mM $NaHCO_3$ and 1% SDS) and reverse-crosslinked at 65 °C for 30 min and then treated with rNase A for 30 min at 37 °C and

Proteinase K at 65 °C for overnight. DNA was purified using AMPureXP beads, and eluted in nuclease-free water. The eluted DNA were further diluted in water and subjected to perform qPCR using primers: *Selplg* E1 F, 5′-CGCACAAACACACACAACTC-3′; *Selplg* E1 R, 5′-TCAGACCCTCCAAACTACCT-3′; *Runx2* E1 F, 5′-AGATCGCTCACTCGACTCAT-3′; *Runx2* E1 R, 5′-CTTCTTCTACTTCCGCCACAC-3′; *Runx2* E2 F, 5′-TCCTTGTCTCTTGCTCTCTTTC-3’; *Runx2* E2 R, 5′-ACAGGTAGTGGCATAGAGGA-3’; *Runx2* E3 F, 5’- GCTGTGTGT TCTTGCTCTTCT-3′; *Runx2* E3 R, 5′-CTAATGAGATGCTGTCGCTGAA-3’; *Runx3* E1 F, 5′- GAGAGCCTTTGAGGTCTCTTTG-3′; *Runx3* E1 R, 5′-CTCAACAGTGCACACCTTCT-3′; *Klf2* P1 F, 5′-AGCAAGGTACCAGGCTACA-3′; *Klf2* P1 R, 5′- TCCCACAGCCTGAAGTCTAA-3’; *Klf2* DE F, 5′-CTATCTCAGGCAACCCAATCA-3′; *Klf2* DE R, 5′-ACCGCTGAAGTTTCTAGGTAAA-3′; Neg F 5′-GCCGCTCTATCATCCGAAAT-3′; Neg R 5′-CCAGCTGCAAGATTAACACAAC-3′. Negative control region was arbitrary selected approximately 40 kb upstream of *Sleplg* E1 site (Fig.5e).

Immunoblot Analysis.

Equivalent cell numbers were lysed in 2X Laemmli sample buffer and boiled for 10 min. The proteins were resolved by NuPAGE 4–12% Bis-Tris gels and transferred onto PVDF membrane in NuPAGE transfer buffer (Invitrogen). Membranes were incubated with primary antibodies: anti-Myc tag (Cell Signaling), anti-Klf2 (EMD Millipore), anti-Runx3 (HRP-conjugated, Santa Cruz Biotechnology), and anti-GAPDH (Santa Cruz Biotechnology). After incubation with HRP-conjugated secondary antibody, target proteins were detected by ECL prime detection kit (GE healthcare) and OdysseyFc Imaging System (LI-COR). The band densities were quantified by ImageStudio Lite software (v.5.2.5; LI-COR).

Statistical analysis.

All RNA-seq and ATAC-seq were performed independently in 3–4 replicates. All graphs represent mean and standard deviations (SD) unless otherwise noted (Prism 8.0, GraphPad). Comparison between two groups was determined by unpaired or paired Student’s *t*-test with a 95% confidence interval. Statistical details of each experiment can be found in the figure legends and specific methods.

Extended Data

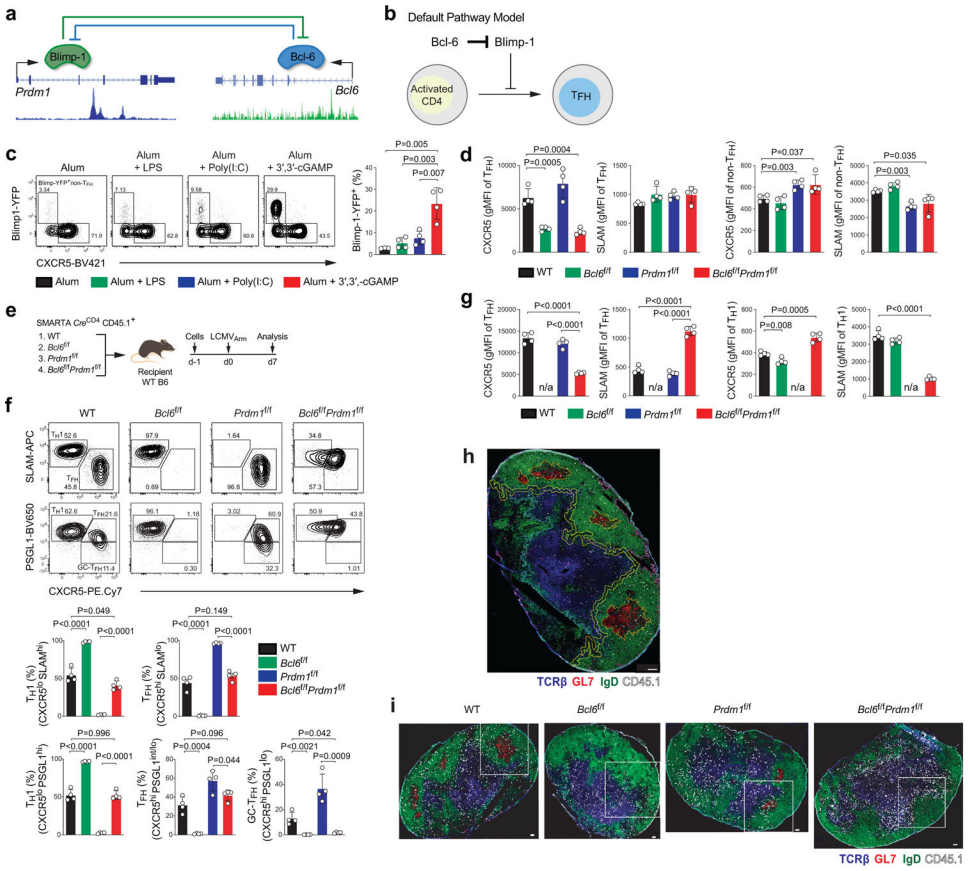

Extended Data Fig. 1. T_{FH} differentiation is not the default pathway.

Related to Fig. 1.

a, Schematic diagram of a mutually antagonistic relationship of Bcl-6 and Blimp-1. UCSC browser tracks from BCL-6 ChIP-seq and Blimp-1 ChIP-seq were indicated below.

b, A null hypothesis of a default T_{FH} differentiation pathway model.

c, SMARTA CD4 T cells were transferred to C57BL/6 host mice, followed by immunization of the host mice with KLH-gp_{61} in alum only, alum + LPS, alum + Poly(I:C), or alum + cGAMP adjuvants, and analyzed 7 days later. Representative flow cytometry of T_{FH} and non-T_{FH} SMARTA cell subsets from draining LNs (dLNs) of KLH-gp_{61} immunized mice. Two independent experiments were performed; each dot represents one mouse (n = 4). Data are mean ± s.d., unpaired two-tailed Student's t-test.

d, Quantification of results from Fig.1b.

e, Schematic of the SMARTA cell transfer system used for $LCMV_{Arm}$ infection. WT, *Bcl6*$^{f/f}$, *Prdm1*$^{f/f}$, and *Bcl6*$^{f/f}$*Prdm1*$^{f/f}$ *Cre*^{CD4} SMARTA $CD4^+$ T cells were transferred to C57BL/6 host mice, followed by infection of the host mice with $LCMV_{Arm}$, and analyzed 7 days later.

f, Representative flow cytometry of GC-T_{FH}, T_{FH} and non-T_{FH} SMARTA cell subsets from spleens of $LCMV_{Arm}$ infected mice in Extended Data Fig.1c. Three independent experiments were performed; each dot represents one mouse (n = 4). Data are mean ± s.d., unpaired two-tailed Student's t-test.

g, Quantification of results from Extended Data Fig.1f.

h, Representative histology section to define GC, B cell zone, T cell zone, and T-B border. T-B border was defined as ±15 μm region at a boundary line of T cell zone and B cell zone. Scale bar, 200 μm. Related to Fig.1g.

i, Histology of draining LNs at d8 after KLH-gp_{61} immunization in Fig. 1d. Blue, TCRβ; red, GL7; green, IgD; white, CD45.1 SMARTA. SMARTA cells were presented with large dots for clarity. Scale bar, 200 μm. Related to Fig.1g.

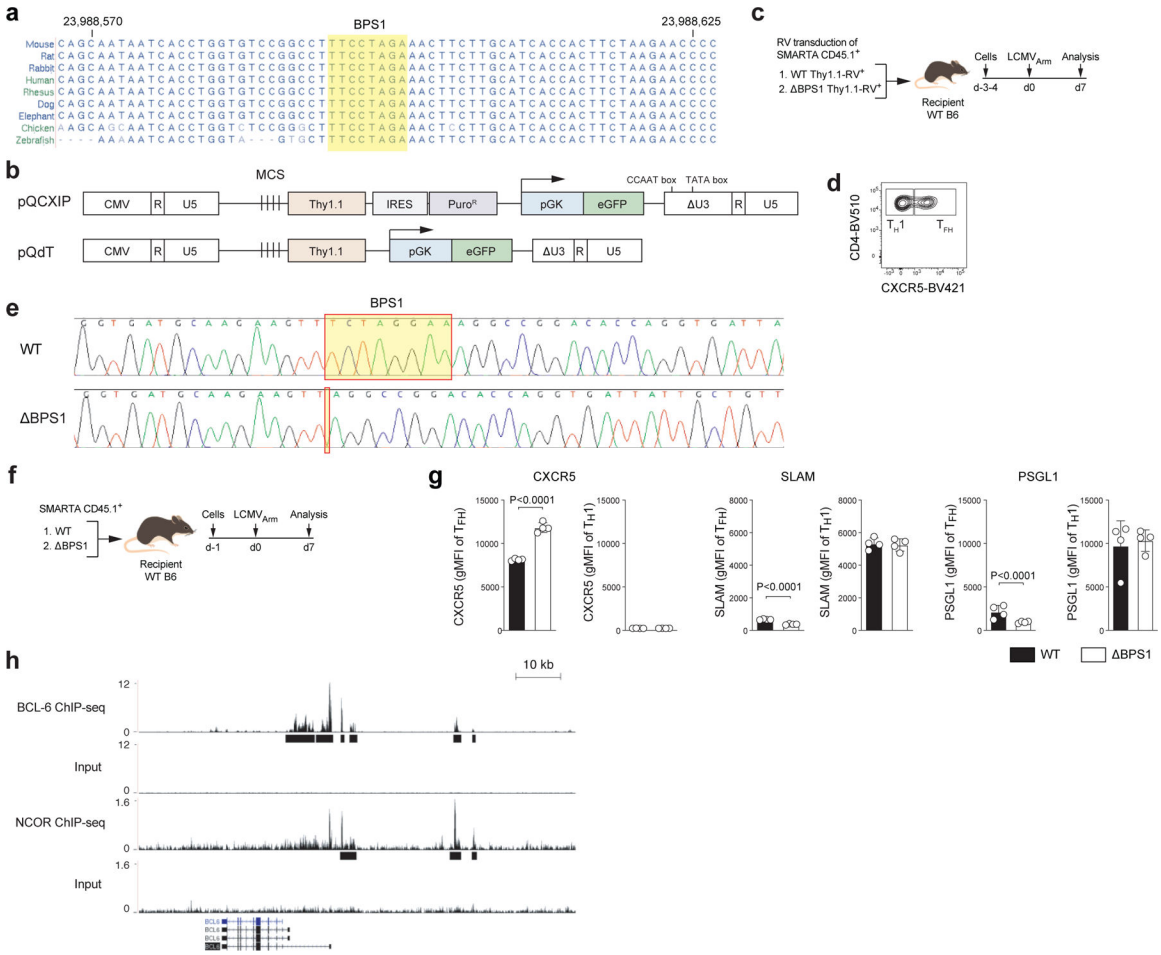

Extended Data Fig. 2. Bcl-6 exhibits direct negative autoregulatory feedback.
Related to Fig. 2.

a, Sequence homology at BPS1 locus between various species. The numbers indicate region of mouse chromosome 19 (mm10).

b, Schematic diagram of self-inactivating (SIN) vectors. pQdT SIN vector were generated from original pQCXIP SIN vector by removing IRES-Puro^R cassette and additional deletion of CCAAT box and TATA box.

c, Schematic of the RV$^+$ SMARTA cell transfer system used for LCMV$_{Arm}$ infection. SMARTA CD4 T cells transduced with WT Thy1.1-RV or ΔBPS1 Thy1.1-RV were adoptively transferred to C57BL/6 host mice, followed by infection of the host mice with LCMV$_{Arm}$, and analyzed 7 days after infection. Related to Fig.2a–b and Extended Data Fig.2d–e.

d, T_{FH} and T_H1 gates used for Fig.2b and Extended Data Fig.2e.

e, Chromatogram of DNA sequencing from WT or ΔBPS1 mouse.

f, Schematic of the SMARTA cell transfer system used for LCMV$_{Arm}$ infection. WT or ΔBPS1 SMARTA CD4 T cells were transferred to C57BL/6 host mice, followed by infection of the host mice with LCMV$_{Arm}$, and analyzed 7 days after infection. Related to Fig. 2c–d.

g, Quantification of expression of CXCR5, SLAM, and PSGL1 in Fig.2d, gated on $CXCR5^{hi}SLAM^{lo}$ T_{FH} or $CXCR5^{lo}SLAM^{hi}$ T_H1 cells. Two independent experiments were performed; each dot represents one mouse (n = 4). Data are mean ± s.d., unpaired two-tailed Student's t-test.

h, Genome-browser tracks depict BCL-6 or NCOR ChIP-Seq peaks at *BCL6* locus from OCI-LY1 cell line. Peak calls indicated below each track.

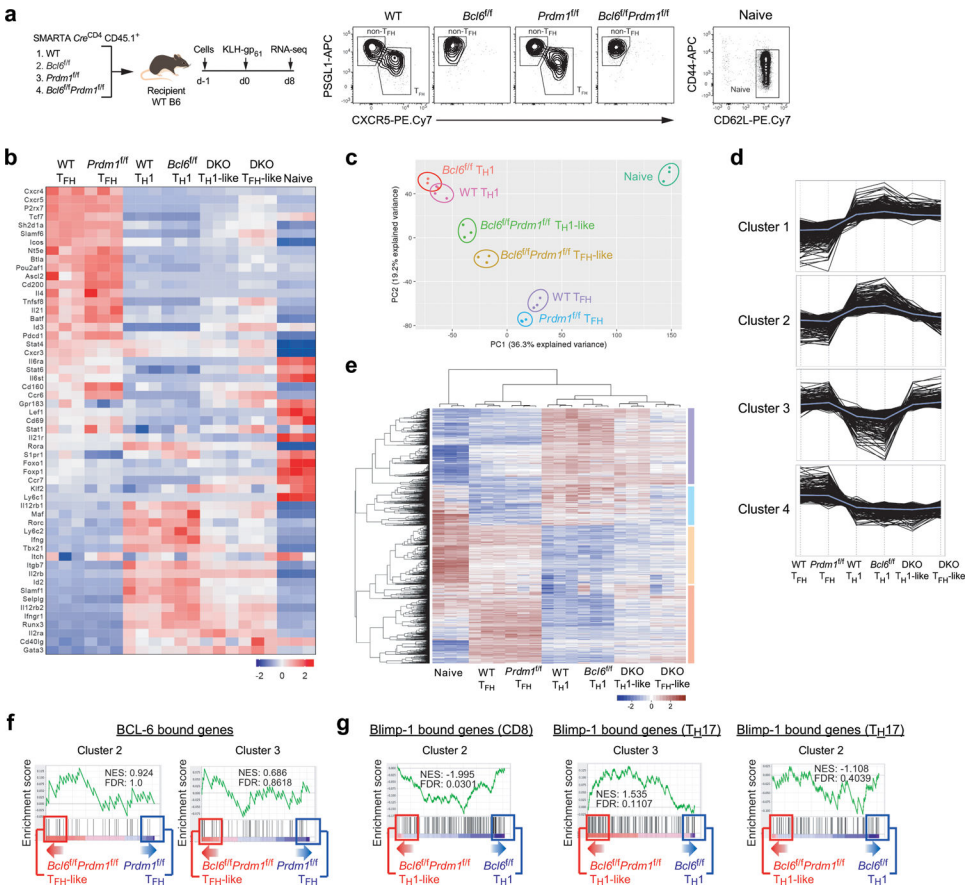

Extended Data Fig. 3. RNA-seq of T_{FH} and non-T_{FH} populations from multiple genetic backgrounds

Related to Fig. 3

a, Schematic of the SMARTA cell transfer system used for RNA-seq analysis in KLH-gp_{61} immunization. Non-T_{FH} ($CXCR5^{lo}PSGL1^{hi}$) populations from WT, *Bcl6*$^{f/f}$ Cre*^{Cd4}*, *Prdm1*$^{f/f}$ Cre^{CD4}, or *Bcl6*$^{f/f}$*Prdm1*$^{f/f}$ Cre*^{Cd4}* SMARTA cells and T_{FH} ($CXCR5^{hi}PSGL1^{lo}$) populations from WT or *Prdm1*$^{f/f}$ Cre^{CD4} SMARTA cells were sorted from C57BL/6 host mice given WT, *Bcl6*$^{f/f}$, *Prdm1*$^{f/f}$, or *Bcl6*$^{f/f}$*Prdm1*$^{f/f}$ Cre^{CD4} SMARTA CD4 T cells, followed by infection of the host mice with KLH-gp_{61} in alum + cGAMP, and analyzed 8 days later. Naive SMARTA cells were isolated as $CD44^{lo}CD62L^{hi}CD45.1^{+}$ from uninfected mice. Representative flow cytometry of T_{FH} and T_H1 subsets from four independent experiments.

b, Heatmap of gene expression of curated T_{FH}-associated genes. Scale, row z-score. DKO, *Bcl6*$^{f/f}$*Prdm1*$^{f/f}$ *Cre*^{CD4}. As a first analysis the effect of *Bcl6*/*Prdm1* double-deficiency on the T_{FH} biology, we assessed expression of a broad curated set of T_{FH}-associated genes across all samples from RNA-seq gene expression profiling. *Bcl6*$^{f/f}$*Prdm1*$^{f/f}$*Cre*^{CD4} T_{FH}-like cells lost expression of positively T_{FH}-associated genes in comparison to WT T_{FH} cells or *Prdm1*$^{f/f}$*Cre*^{CD4} T_{FH} cells. Conversely, *Bcl6*$^{f/f}$*Prdm1*$^{f/f}$*Cre*^{CD4} T_H1-like cells had a gene expression profile different from WT T_H1 or *Bcl6*$^{f/f}$*Cre*^{CD4} T_H1 cells.

c, Principal component analysis of differential gene expression from RNA-seq of $LCMV_{Arm}$ infection. Principal component analysis provided similar findings as (b), supporting the

overall hypothesis that T_{FH} is not a default differentiation pathway of $CD4^+$ T cells and Bcl-6 has important activities beyond inhibition of *Prdm1*.

d, Gene expression changes were clustered by K-means clustering analysis (K=10) of $LCMV_{Arm}$ infection.

e, Hierarchical clustering analysis of genes upregulated or downregulated in T_{FH} cells relative to their expression in T_H1 cells (1.4-fold cut off, Adj. P <0.05) of $LCMV_{Arm}$ infection shown in Fig.3c. Scale, row z-score.

f, GSEA of BCL-6 bound genes from human tonsillar GC-T_{FH} compared to Cluster 2 genes (left) or Cluster 3 genes (right) differentially expressed between *Bcl6*$^{f/f}$*Prdm1*$^{f/f}$ T_{FH}-like cells and *Prdm1*$^{f/f}$ T_{FH} cells. NES, normalized enrichment score; FDR, false discovery rate.

g, GSEA of Blimp-1 bound genes from CD8 and T_H17 cells in comparison of Cluster 2 and Cluster 3 genes differentially expressed between *Bcl6*$^{f/f}$*Prdm1*$^{f/f}$ T_H1-like cells and *Bcl6*$^{f/f}$ T_H1 cells.

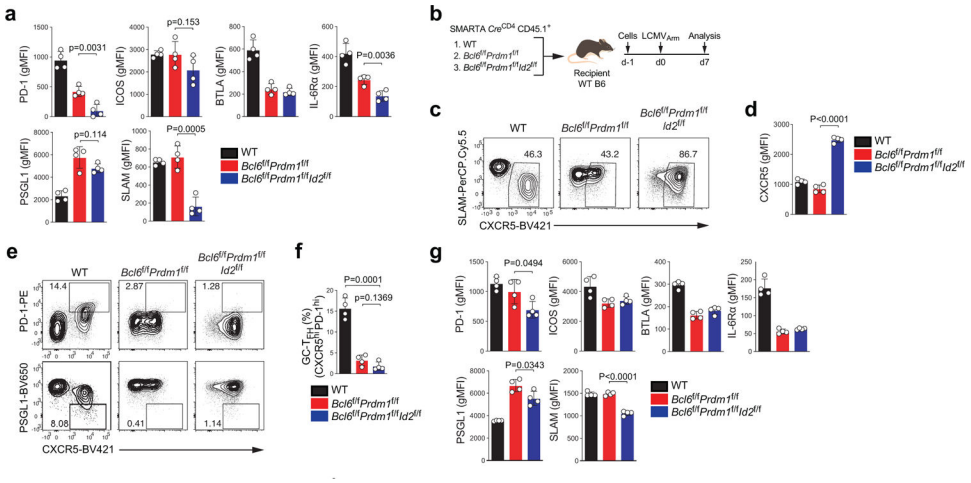

Extended Data Fig. 4. Bcl-6 drives CXCR5 expression via repression of Id2-E2A pathway
Related to Fig. 4

a, Quantification of GC-T_{FH} core signature markers in SMARTA cells from dLNs of KLH-gp_{61} immunized mice in Fig. 4d.

b, Schematic of the SMARTA cell transfer system used for $LCMV_{Arm}$ infection. WT, *Bcl6*$^{f/f}$ *Prdm1*$^{f/f}$, or *Bcl6*$^{f/f}$ *Prdm1*$^{f/f}$ *Id2*$^{f/f}$ *Cre*^{CD4} SMARTA CD4 T were transferred to C57BL/6 host mice, followed by infection of the host mice with $LCMV_{Arm}$, and analyzed 7 days later. Related to Fig 4g and Extended Data Fig. 4c–g.

c,e, Representative flow cytometry of T_{FH} and GC-T_{FH} SMARTA cell subsets from spleen of $LCMV_{Arm}$ infected mice. Two independent experiments performed; each dot represents one mouse (n = 4). Data are mean ± s.d., unpaired two-tailed Student's t-test.

d, Quantification of expression of CXCR5 in Extended Data Fig. 4c, gated on SMARTA cells.

f, Quantification of frequency of CXCR5^{hi}PD1^{hi} GC-T_{FH} cells in Extended Data Fig.4e, gated on SMARTA cells.

g, Quantification of GC-T_{FH} core signature markers in Extended Data Fig.4e, gated on SMARTA cells.

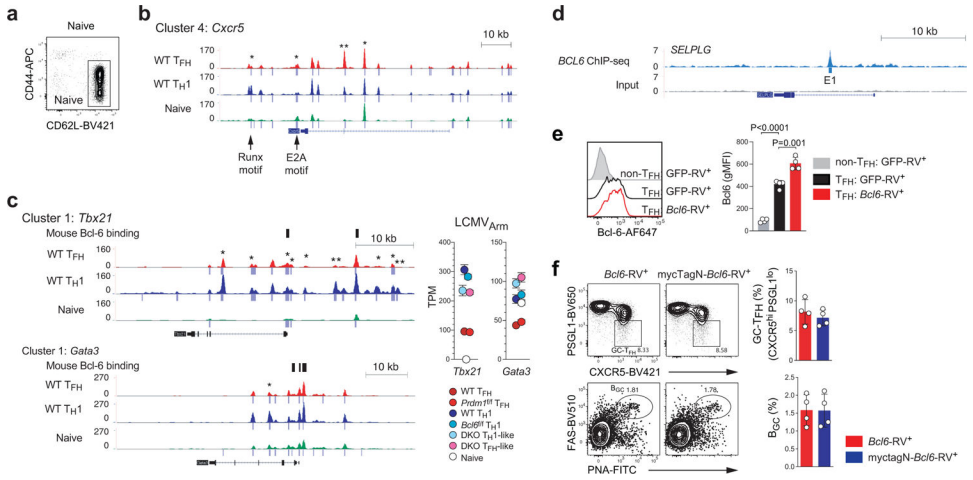

Extended Data Fig. 5. ATAC-seq of T_{FH} and non-T_{FH} populations from multiple genetic backgrounds.

Related to Fig. 5

a, Representative flow cytometry of naive SMARTA cells ($CD44^{lo}CD62L^{hi}CD45.1^{+}$) used for ATAC-seq analysis.

b, Genome-browser tracks depict ATAC-seq chromatin accessibility at *Cxcr5* locus. Peak calls indicated below each track. * indicates DEseq2 raw $p \leq 0.05$ in comparison between WT T_{FH} and T_H1.

c, Genome-browser tracks depict ATAC-seq chromatin accessibility at *Tbx21* and *Gata3* loci.

Peak calls indicated below each track. Bcl-6 liftover peaks from human to mouse reference genome are indicated. * and ** indicate DEseq2 raw p-val 0.05 and 0.01, respectively, in comparison between WT T_{FH} and T_H1. Gene expressions from RNA-seq data of $LCMV_{Arm}$ infected mice are graphed. DKO, $Bcl6^{f/f}Prdm1^{f/f}$ Cre^{CD4}.

d, Genome-browser tracks depict BCL-6 ChIP-Seq peaks at *SELPLG* locus. Peak calls indicated below the track.

e, Representative flow cytometry and quantification of the level of Bcl-6 in RV^{+} T_{FH} or non-T_{FH} SMARTA cell subsets from spleen of $LCMV_{Arm}$ infected mice. SMARTA CD4 T cells transduced with GFP-RV or *Bcl6*-RV were transferred to C57BL/6 host mice, followed by infection of the host mice with $LCMV_{Arm}$, and analyzed 3 days after infection. Non-T_{FH}: GFP-RV^{+} and T_{FH}: GFP-RV^{+} indicate the expression level of endogenous Bcl-6 in each population. Each dot represents one mouse (n = 4). Data are mean s.d., unpaired two-tailed Student's t-test.

f, Representative flow cytometry and quantification of GC-T_{FH} and B_{GC} subpopulations from spleen of $LCMV_{Arm}$ infected mice. $Bcl6^{f/f}$ Cre^{CD4} SMARTA CD4 T cells transduced with *Bcl6*-RV or myctagN-*Bcl6*-RV were transferred to $Bcl6^{f/f}$ Cre^{CD4} host mice, followed by infection of the host mice with $LCMV_{Arm}$, and analyzed 8 days after infection. We validated that an myctagN-*Bcl6*-RV was functionally comparable with non-tagged *Bcl6*-RV (*Bcl6*-RV), based on myctagN-*Bcl6*-RV rescue of T_{FH} differentiation and B cell help function of $Bcl6^{f/f}$ Cre^{CD4} CD4 T cells in LCMV infected mice. Each dot represents one mouse (n = 4). Data are mean s.d.

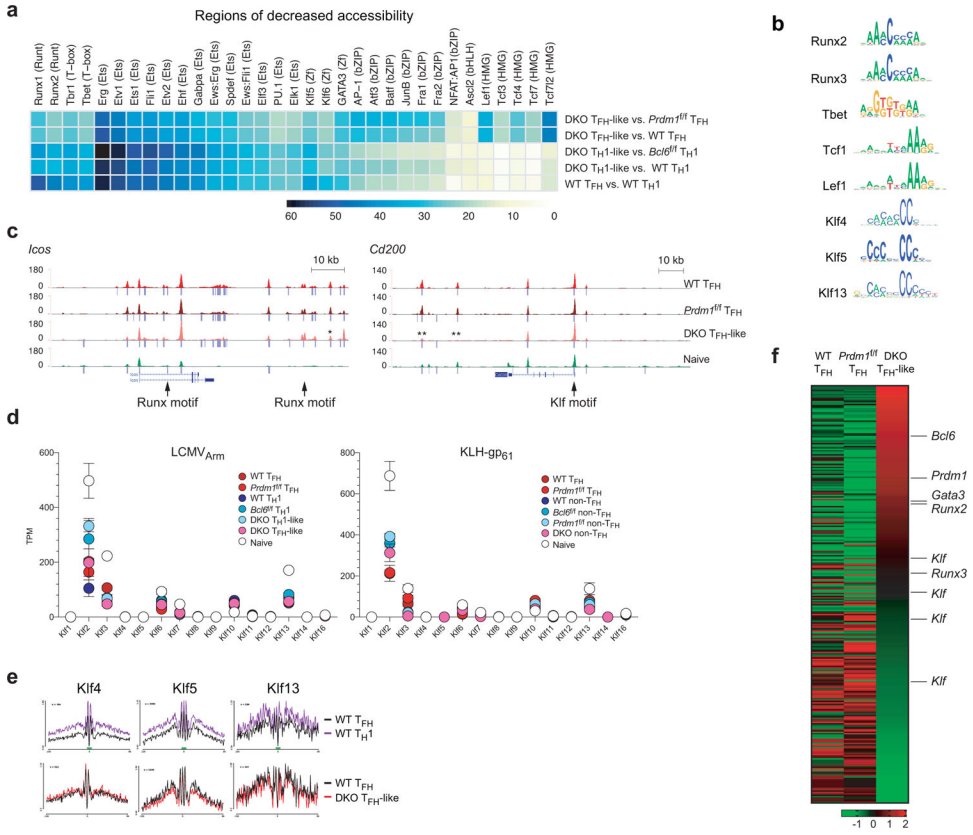

Extended Data Fig. 6. Identification of candidate TFs.

Related to Fig. 6

a, Heatmap plots representing the frequencies of the most enriched TF motifs in regions in decreased accessibility (relatively less open in first group than second group, DEseq2 raw p-val < 0.05). Scale, motif frequencies (%). Related to Fig.6b.

b, Motif analysis of the center of TF footprint (green bar) in Fig.6c and Extended Data Fig.6e from ATAC-seq reads.

c, Genome-browser tracks depict ATAC-seq chromatin accessibility and TF occupancy at *Icos* and *Cd200* loci. Peak calls indicated below each track. ** indicates DEseq2 raw p-val ≤ 0.01 in comparison between *Bcl6*$^{f/f}$*Prdm1*$^{f/f}$ *Cre*^{CD4} T_{FH}-like and *Prdm1*$^{f/f}$ *Cre*^{CD4} T_{FH}.

d, Gene expression of *Klf* genes from RNA-seq data of $LCMV_{Arm}$ infected mice or KLH-gp61 immunized mice.

e, TF footprints derived from ATAC-seq reads over representative TF motifs within accessible ATAC-seq regions.

f, Heatmap plots of relative PageRank scores. Scale, row z-score.

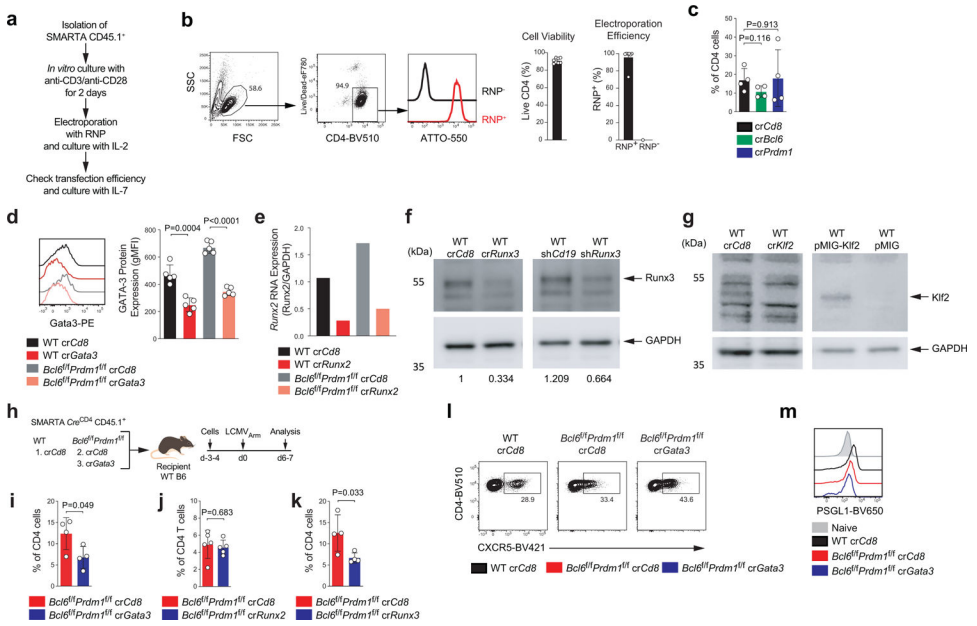

Extended Data Fig. 7. CRISPR/Cas9-mediated gene knockdown of SMARTA cells.
Related to Fig. 7

a, Schematic of the CRISPR/Cas9-mediated gene knockdown of SMARTA cell system. Details are in the Method section.

b, Representative flow cytometry of RNP transfection from more than four independent experiment; each dot represents one RNP+ group (n = 9). Data are mean ± s.d. Quantification of cell viability and transfection efficiency of RNP^+ and RNP^- (electroporation without RNP) SMARTA cells.

c, Frequency of $crRNA^+$ $CD45.1^+$ SMARTA cells among total CD4 T cells from spleen of $LCMV_{Arm}$ infected mice in Fig.7a. Two independent experiments were performed; each dot represents one $crRNA^+$ group (n = 4). Data are mean ± s.d., unpaired two-tailed Student's t-test.

d,e,f,g, WT or *Bcl6*$^{f/f}$*Prdm1*$^{f/f}$ *Cre*^{CD4} SMARTA CD4 T cells transfected with cr*Cd8*, cr*Gata3*, cr*Runx2*, cr*Runx3*, and cr*Klf2* were transferred to C57BL/6 host mice, followed by infection with $LCMV_{Arm}$ (e,f,g) or immunization with KLH-gp_{61} (d) of the host mice, and analyzed 6–7 days later. $crRNA^+$ SMARTA cells were FACS sorted from spleens ($LCMV_{Arm}$ infection) or dLN (KLH-gp_{61} immunization) of host mice. Gene knockdown efficiencies were measured by flow cytometry (d), mRNA qPCR (e), or Western blot analysis (f,g). sh*Runx3*-RV^+ SMATRA cells and pMIG-Klf2-RV^+ SMARTA cells were used as positive controls. Two independent experiments were performed; Each dot represents one mouse (n = 5). Data are mean ± s.d., unpaired two-tailed Student's t-test. Details are in the Method section.

h, Schematic of the CRISPR/Cas9-mediated gene knockdown of SMARTA cell system used for testing *Gata3* in $LCMV_{Arm}$ infection. WT or *Bcl6*$^{f/f}$*Prdm1*$^{f/f}$ *Cre*^{CD4} SMARTA CD4 T cells transfected with cr*Cd8* or cr*Gata3* were transferred to C57BL/6 host mice, followed by infection of the host mice with $LCMV_{Arm}$, and analyzed 6–7 days later. Related to Fig.7c and Extended Data Fig.7i,l,m.

i,j,k, Frequency of $crRNA^+$ $CD45.1^+$ SMARTA cells among total CD4 T cells from spleen of $LCMV_{Arm}$ infected mice in Fig.7d and Extended Data Fig.7h. Two (i) or three (j,k) independent experiments were performed; each dot represents one mouse (n = 4). Data are mean ± s.d., unpaired two-tailed Student's t-test.

l, Representative flow cytometry of T_{FH} SMARTA cell subsets from spleen of $LCMV_{Arm}$ infected mice in Extended Data Fig.7h. Two independent experiments were performed; Each dot represents one mouse (n = 4). Data are mean ± s.d., unpaired two-tailed Student's t-test.

m, Quantification of expression of PSGL1 in Extended Data Fig.7h, gated on SMARTA cells. $CD44^{lo}$ naive CD4 T cells were used as a negative control.

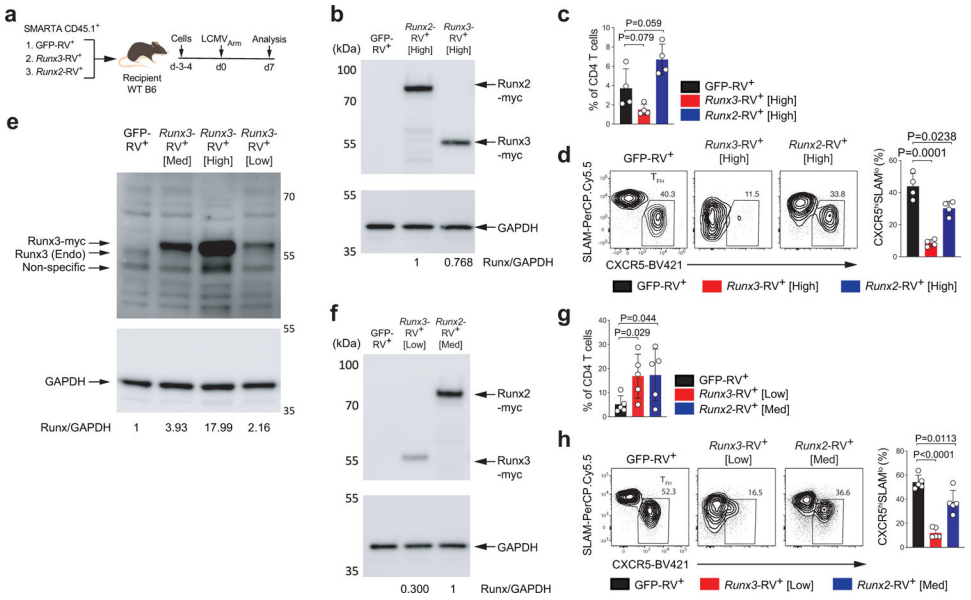

Extended Data Fig. 8. Identification of *Runx2*, *Runx3*, and *Gata3* as repressors of T_{FH} genes, acting downstream of Bcl-6.

Related to Fig. 7

a, Schematic of the RV^+ SMARTA cell transfer system used for $LCMV_{Arm}$ infection. WT SMARTA CD4 T cells transduced with pMIG (GFP-RV^+), pMIG-Runx3myc (*Runx3*-RV^+), or pMIG-Runx2myc (*Runx2*-RV^+) were transferred to C57BL/6 host mice, followed by infection of the host mice with $LCMV_{Arm}$, and analyzed 7 days after infection. Related to Fig.7i–j and Extended Data Fig.7o–u.

b, Total GFP^+ RV^+ SMARTA cells [RV^+ high] were FACS sorted from *in vitro* culture. Whole cell lysates were analyzed by immunoblotting using anti-myc tag and anti-GAPDH antibodies. Relative Runx expressions are indicated.

c, SMARTA CD4 T cells transduced with pMIG (GFP-RV^+), pMIG-Runx3myc (*Runx3*-RV^+ [High]), or pMIG-Runx2myc (*Runx2*-RV^+ [High]) were transferred to C57BL/6 host mice, followed by infection of the host mice with $LCMV_{Arm}$, and analyzed 7 days later. Frequency of $CD45.1^+$ SMARTA cells among total CD4 T cells from spleen of $LCMV_{Arm}$ infected mice. Two independent experiments were performed; each dot represents one mouse (n = 4). Data are mean ± s.d., unpaired two-tailed Student's t-test.

d, Representative flow cytometry of T_{FH} RV^+ [High] SMARTA cell subsets from spleen of $LCMV_{Arm}$ infected mice. Quantification of results from left panels.

e, Bottom 10% [Low], bottom 10–30% [Med] and remaining 30–100% [High] GFP^+ Runx3-RV^+ SMARTA cells, and total GFP^+ RV^+ SMARTA cells were FACS sorted from *in vitro* culture. Whole cell lysates were analyzed by immunoblotting using anti-Runx3 and anti-GAPDH antibodies. Relative Runx expressions are indicated.

f, Bottom 10% GFP^+ Runx3-RV^+ (Runx3-RV^+ [Low]), bottom 30% GFP^+ Runx2-RV^+ (Runx2-RV^+ [Med]), and total GFP^+ RV^+ (GFP-RV^+) SMARTA cells were FACS sorted from *in vitro* culture. Whole cell lysates were analyzed by immunoblotting using anti-myc tag and anti-GAPDH antibodies. Relative Runx expressions are indicated.

g, SMARTA CD4 T cells transduced with pMIG (GFP-RV^+), pMIG-Runx3myc (*Runx3*-RV^+ [Low]), or pMIG-Runx2myc (*Runx2*-RV^+ [Med]) were transferred to C57BL/6 host mice,

followed by infection of the host mice with $LCMV_{Arm}$, and analyzed 7 days later. Frequency of $CD45.1^+$ SMARTA cells among total CD4 T cells from spleen of $LCMV_{Arm}$ infected mice. Two independent experiments were performed; each dot represents one mouse (n = 5). Data are mean ± s.d., unpaired two-tailed Student's t-test.

h, Representative flow cytometry of T_{FH} Runx3-RV^+ [Low] and Runx2-RV^+ [Med] SMARTA cell subsets from spleen of $LCMV_{Arm}$ infected mice. Quantification of results from left panels.

h, Representative flow cytometry of T_{FH} Runx3-RV^+ [Low] and Runx2-RV^+ [Med] SMARTA cell subsets from spleen of $LCMV_{Arm}$ infected mice. Quantification of results from left panels.

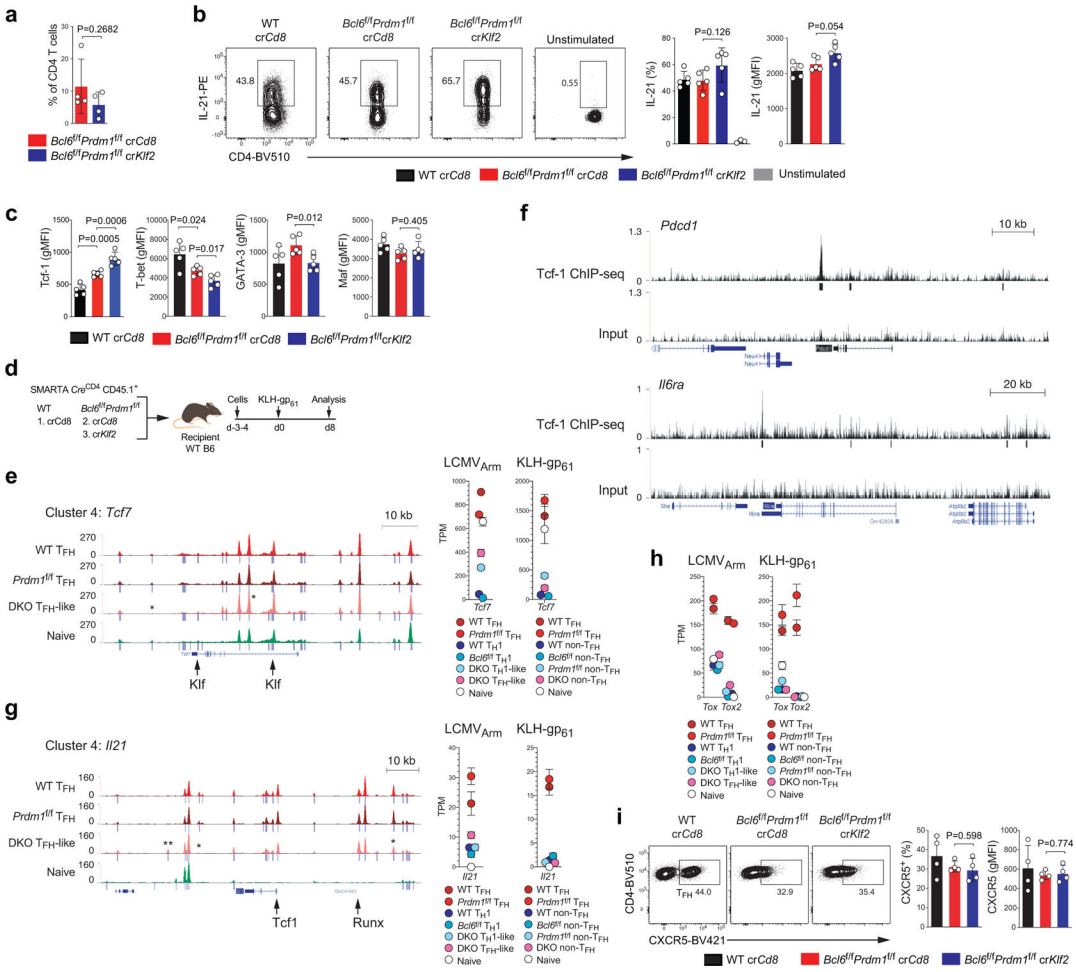

Extended Data Figure 9. Identification of *Klf2* as a repressor, acting downstream of Bcl-6 regulating major of T_{FH} genes.

Related to Fig.8

a-c, WT or *Bcl6*$^{f/f}$*Prdm1*$^{f/f}$ *Cre*^{Cd4} SMARTA CD4 T cells transfected with cr*Cd8* or cr*Klf2* were transferred to C57BL/6 host mice, followed by infection of the host mice with $LCMV_{Arm}$, and analyzed 6–7 days later (n=4–5 mice per group). (a) Frequency of CD45.1$^+$ SMARTA cells among total CD4 T cells from spleen of $LCMV_{Arm}$ infected mice. (b) Representative flow cytometry of gp_{66}-restimulated IL-21$^+$ SMARTA cells. Quantification of results from left panels. (c) Quantification of expression of Tcf-1, T-bet, GATA-3, and Maf, gated on SMARTA cells. Three independent experiments were performed; each dot represents one mouse (a, n = 4; b-c, n = 5). Data are mean ± s.d., unpaired two-tailed Student's t-test. Related to Fig.8a–c.

d, Schematic of the CRISPR/Cas9-mediated gene knockdown of SMARTA cell system used for testing *Klf2* in KLH-gp_{61} immunization. WT or *Bcl6*$^{f/f}$*Prdm1*$^{f/f}$ *Cre*^{CD4} SMARTA CD4 T cells transfected with cr*Cd8* or cr*Klf2* were transferred to C57BL/6 host mice, followed by immunization of the host mice with KLH-gp_{61} and alum + cGAMP, and analyzed 8 days later. Related to Fig. 8d–f.

e,g, Genome-browser tracks depict ATAC-seq chromatin accessibility and TF occupancy. Peak calls indicated below each track. * and ** indicate DEseq2 raw p-val ≤ 0.05 and ≤

0.01, respectively, in comparison between *Bcl6*$^{f/f}$*Prdm1*$^{f/f}$ Cre^{CD4} T_{FH}-like and *Prdm1*$^{f/f}$ Cre^{CD4} T_{FH}. Gene expression from RNA-seq data of $LCMV_{Arm}$ infected mice and KLH-gp_{61} immunized mice are graphed.

f, Genome-browser tracks depict Tcf1 ChIP-Seq peaks at *Pdcd1* and *IL6ra* loci from murine T_{FH} cells.

h, Gene expression of Tox and Tox2 from RNA-seq data of $LCMV_{Arm}$ infected mice or KLH-gp_{61} immunized mice.

i, Representative flow cytometry of T_{FH} cells, gated on SMARTA cells from spleens of $LCMV_{Arm}$ infected mice (n=4 mice per group) in Fig. 8a. Quantification of results from left panels.

Supplementary Material

Refer to Web version on PubMed Central for supplementary material.

ACKNOWLEDGEMENTS

We thank C. Kim, L. Boggeman, D. Hinz, and C. Dillingham of LJI Flow Cytometry Core Facility for cell sorting, J. Greenbaum and A. Sethi of LJI Bioinformatics core for bioinformatics analysis, G. Seumois and J. Day of LJI Sequencing core, and K. Jepsen of UCSD IGM sequencing core for consultation. We thank MaxCyte, Inc. for generously providing the MaxCyte ATX electroporator and reagents. This work was funded by grants from the USA National Institutes of Health (NIH), including National Institute of Allergy and Infectious Diseases (NIAID) U19 AI109976 and NIAID R01 AI072543, NIH S10 RR027366 (LJI), and internal La Jolla Institute institutional funds to S.C.

REFERENCES

1. Crotty S T Follicular Helper Cell Biology: A Decade of Discovery and Diseases. Immunity 50, 1132–1148 (2019). [PubMed: 31117010]
2. Vinuesa CG, Linterman MA, Yu D & MacLennan ICM Follicular Helper T Cells. Annu. Rev. Immunol 34, 335–368 (2016). [PubMed: 26907215]
3. Johnston RJ et al. Bcl6 and Blimp1 Are Reciprocal and Antagonistic Regulators of T Follicular Helper Cell Differentiation. Science 325, 1006–1010 (2009). [PubMed: 19608860]
4. Yu D et al. The Transcriptional Repressor Bcl-6 Directs T Follicular Helper Cell Lineage Commitment. Immunity 31, 457–468 (2009). [PubMed: 19631565]
5. Nurieva RI et al. Bcl6 Mediates the Development of T Follicular Helper Cells. Science 325, 1001–1005 (2009). [PubMed: 19628815]
6. Crotty S T follicular helper cell differentiation, function, and roles in disease. Immunity 41, 529–542 (2014). [PubMed: 25367570]
7. Ise W et al. The transcription factor BATF controls the global regulators of class-switch recombination in both B cells and T cells. Nature Immunology 12, 536–543 (2011). [PubMed: 21572431]
8. Kroenke MA et al. Bcl6 and Maf Cooperate To Instruct Human Follicular Helper CD4 T Cell Differentiation. J. Immunol 188, 3734–3744 (2012). [PubMed: 22427637]
9. Johnston RJ, Choi YS, Diamond JA, Yang JA & Crotty S STAT5 is a potent negative regulator of TFH cell differentiation. J. Exp. Med 209, 243–250 (2012). [PubMed: 22271576]
10. Choi YS, Eto D, Yang JA, Lao C & Crotty S Cutting edge: STAT1 is required for IL-6-mediated Bcl6 induction for early follicular helper cell differentiation. J. Immunol 190, 3049–3053 (2013). [PubMed: 23447690]
11. Wang H et al. The transcription factor Foxp1 is a critical negative regulator of the differentiation of follicular helper T cells. Nature Immunology 15, 667–675 (2014). [PubMed: 24859450]

12. Stone EL et al. ICOS coreceptor signaling inactivates the transcription factor FOXO1 to promote Tfh cell differentiation. Immunity 42, 239–251 (2015). [PubMed: 25692700]
13. Lee J-Y et al. The transcription factor KLF2 restrains CD4+ T follicular helper cell differentiation. Immunity 42, 252–264 (2015). [PubMed: 25692701]
14. Weber JP et al. ICOS maintains the T follicular helper cell phenotype by down-regulating Krüppel-like factor 2. J. Exp. Med 212, 217–233 (2015). [PubMed: 25646266]
15. Krishnamoorthy V et al. The IRF4 Gene Regulatory Module Functions as a Read-Write Integrator to Dynamically Coordinate T Helper Cell Fate. Immunity 47, 481–497.e7 (2017). [PubMed: 28930660]
16. Kim CJ et al. The Transcription Factor Ets1 Suppresses T Follicular Helper Type 2 Cell Differentiation to Halt the Onset of Systemic Lupus Erythematosus. Immunity 49, 1034–1048.e8 (2018). [PubMed: 30566881]
17. Lahmann A et al. Bach2 Controls T Follicular Helper Cells by Direct Repression of Bcl-6. J. Immunol 202, 2229–2239 (2019). [PubMed: 30833348]
18. Geng J et al. Bach2 Negatively Regulates T Follicular Helper Cell Differentiation and Is Critical for CD4+ T Cell Memory. J. Immunol ji1801626 (2019). doi:10.4049/jimmunol.1801626
19. Choi YS et al. LEF-1 and TCF-1 orchestrate TFH differentiation by regulating differentiation circuits upstream of the transcriptional repressor Bcl6. Nature Immunology 16, 980–990 (2015). [PubMed: 26214741]
20. Xu L et al. The transcription factor TCF-1 initiates the differentiation of TFH cells during acute viral infection. Nature Immunology 16, 1–11 (2015). [PubMed: 25521670]
21. Wu T et al. TCF1 Is Required for the T Follicular Helper Cell Response to Viral Infection. Cell Rep 12, 2099–2110 (2015). [PubMed: 26365183]
22. Shaw LA et al. Id2 reinforces TH1 differentiation and inhibits E2A to repress TFH differentiation. Nature Immunology 17, 834–843 (2016). [PubMed: 27213691]
23. Liu X et al. Transcription factor achaete-scute homologue 2 initiates follicular T-helper-cell development. Nature 507, 513–518 (2014). [PubMed: 24463518]
24. Hatzi K et al. BCL6 orchestrates Tfh cell differentiation via multiple distinct mechanisms. J. Exp. Med 212, 539–553 (2015). [PubMed: 25824819]
25. Liu X et al. Genome-wide Analysis Identifies Bcl6-Controlled Regulatory Networks during T Follicular Helper Cell Differentiation. Cell Rep 14, 1735–1747 (2016). [PubMed: 26876184]
26. Crotty S, Johnston RJ & Schoenberger SP Effectors and memories: Bcl6 and Blimp1 in T and B lymphocyte differentiation. Nature Immunology 11, 114–120 (2010). [PubMed: 20084069]
27. Crotty S Follicular Helper CD4 T Cells (TFH). Annu. Rev. Immunol 29, 621–663 (2011). [PubMed: 21314428]
28. Nance JP et al. Bcl6 middle domain repressor function is required for T follicular helper cell differentiation and utilizes the corepressor MTA3. Proc. Natl. Acad. Sci. U.S.A 112, 13324–13329 (2015). [PubMed: 26460037]
29. Xie MM et al. Bcl6 promotes follicular helper T-cell differentiation and PD-1 expression in a Blimp1-independent manner in mice. European Journal of Immunology 47, 1136–1141 (2017). [PubMed: 28586108]
30. Mendez LM et al. CtBP is an essential corepressor for BCL6 autoregulation. Mol. Cell. Biol 28, 2175–2186 (2008). [PubMed: 18212045]
31. Huynh KD & Bardwell VJ The BCL-6 POZ domain and other POZ domains interact with the co-repressors N-CoR and SMRT. Oncogene 17, 2473–2484 (1998). [PubMed: 9824158]
32. Bartfeld D et al. DNA Recognition by the RUNX1 Transcription Factor Is Mediated by an Allosteric Transition in the RUNT Domain and by DNA Bending. Structure 10, 1395–1407 (2002). [PubMed: 12377125]
33. Hiramatsu Y et al. c-Maf activates the promoter and enhancer of the IL-21 gene, and TGF-beta inhibits c-Maf-induced IL-21 production in CD4+ T cells. J Leukoc Biol 87, 703–712 (2010). [PubMed: 20042469]
34. Sahoo A et al. Batf is important for IL-4 expression in T follicular helper cells. Nat Commun 6, 7997 (2015). [PubMed: 26278622]

35. Hatzi K et al. A Hybrid Mechanism of Action for BCL6 in B Cells Defined by Formation of Functionally Distinct Complexes at Enhancers and Promoters. Cell Rep 4, 578–588 (2013). [PubMed: 23911289]
36. Pasqualucci L & Dalla Favera R Genetics of diffuse large B-cell lymphoma. Blood 131, 2307–2319 (2018). [PubMed: 29666115]
37. Kusam S, Toney LM, Sato H & Dent AL Inhibition of Th2 Differentiation and GATA-3 Expression by BCL-6. J. Immunol 170, 2435–2441 (2003). [PubMed: 12594267]
38. Kwon H-K, Chen H-M, Mathis D & Benoist C Different molecular complexes that mediate transcriptional induction and repression by FoxP3. Nature Immunology 486, 549–1248 (2017).
39. Ciofani M et al. A validated regulatory network for Th17 cell specification. Cell 151, 289–303 (2012). [PubMed: 23021777]
40. Iwata S et al. The Transcription Factor T-bet Limits Amplification of Type I IFN Transcriptome and Circuitry in T Helper 1 Cells. Immunity 46, 983–991.e4 (2017). [PubMed: 28623086]
41. Vahedi G et al. Helper T-cell identity and evolution of differential transcriptomes and epigenomes. Immunol. Rev 252, 24–40 (2013). [PubMed: 23405893]
42. Oxenius A, Bachmann MF, Zinkernagel RM & Hengartner H Virus-specific major MHC class II-restricted TCR-transgenic mice: effects on humoral and cellular immune responses after viral infection. European Journal of Immunology 28, 390–400 (1998). [PubMed: 9485218]
43. Kaji T et al. Distinct cellular pathways select germline-encoded and somatically mutated antibodies into immunological memory. J. Exp. Med 209, 2079–2097 (2012). [PubMed: 23027924]
44. Shapiro-Shelef M et al. Blimp-1 is required for the formation of immunoglobulin secreting plasma cells and pre-plasma memory B cells. Immunity 19, 607–620 (2003). [PubMed: 14563324]
45. Rutishauser RL et al. Transcriptional repressor Blimp-1 promotes CD8(+) T cell terminal differentiation and represses the acquisition of central memory T cell properties. Immunity 31, 296–308 (2009). [PubMed: 19664941]
46. Wang D et al. The Transcription Factor Runx3 Establishes Chromatin Accessibility of cis - Regulatory Landscapes that Drive Memory Cytotoxic T Lymphocyte Formation. Immunity 48, 659–674.e6 (2018). [PubMed: 29669249]
47. Rosenbauer F et al. Lymphoid cell growth and transformation are suppressed by a key regulatory element of the gene encoding PU.1. Nat. Genet 38, 27–37 (2006). [PubMed: 16311598]
48. Montague TG, Cruz JM, Gagnon JA, Church GM & Valen E CHOPCHOP: a CRISPR/Cas9 and TALEN web tool for genome editing. Nucleic Acids Res 42, W401–7 (2014). [PubMed: 24861617]
49. Seumois G et al. Transcriptional Profiling of Th2 Cells Identifies Pathogenic Features Associated with Asthma. J. Immunol 197, 655–664 (2016). [PubMed: 27271570]
50. Benjamini Y & Hochberg Y Controlling the False Discovery Rate: A Practical and Powerful Approach to Multiple Testing. Journal of the Royal Statistical Society: Series B (Methodological) 57, 289–300 (1995).
51. Raykov YP, Boukouvalas A, Baig F & Little MA What to Do When K-Means Clustering Fails: A Simple yet Principled Alternative Algorithm. PLoS ONE 11, e0162259 (2016). [PubMed: 27669525]
52. Subramanian A et al. Gene set enrichment analysis: a knowledge-based approach for interpreting genome-wide expression profiles. Proc. Natl. Acad. Sci. U.S.A 102, 15545–15550 (2005). [PubMed: 16199517]
53. Jain R et al. Interleukin-23-Induced Transcription Factor Blimp-1 Promotes Pathogenicity of T Helper 17 Cells. Immunity 44, 131–142 (2016). [PubMed: 26750311]
54. Mackay LK et al. Hobit and Blimp1 instruct a universal transcriptional program of tissue residency in lymphocytes. Science 352, 459–463 (2016). [PubMed: 27102484]
55. Masson F et al. Id2-Mediated Inhibition of E2A Represses Memory CD8(+) T Cell Differentiation. J. Immunol 190, 4585–4594 (2013). [PubMed: 23536629]
56. Yu B et al. Epigenetic landscapes reveal transcription factors that regulate CD8(+) T cell differentiation. Nature Immunology 18, 573–582 (2017). [PubMed: 28288100]

57. Anders S, Pyl PT & Huber W HTSeq-a Python framework to work with high-throughput sequencing data. Bioinformatics 31, 166–169 (2015). [PubMed: 25260700]

58. Pedregosa F et al. Scikit-learn: Machine Learning in Python. Journal of Machine Learning Research 12, 2825–2830 (2011).

59. Wingender E, Schoeps T, Haubrock M, Krull M & Dönitz J TFClass: expanding the classification of human transcription factors to their mammalian orthologs. Nucleic Acids Res 46, D343–D347 (2018). [PubMed: 29087517]

60. Li Z et al. Identification of transcription factor binding sites using ATAC-seq. Genome Biol 20, 45 (2019). [PubMed: 30808370]

61. Stormo GD Modeling the specificity of protein-DNA interactions. Quant Biol 1, 115–130 (2013). [PubMed: 25045190]

62. Li F et al. Ezh2 programs TFH differentiation by integrating phosphorylation-dependent activation of Bcl6 and polycomb-dependent repression of p19Arf. Nat Commun 9, 5452 (2018). [PubMed: 30575739]

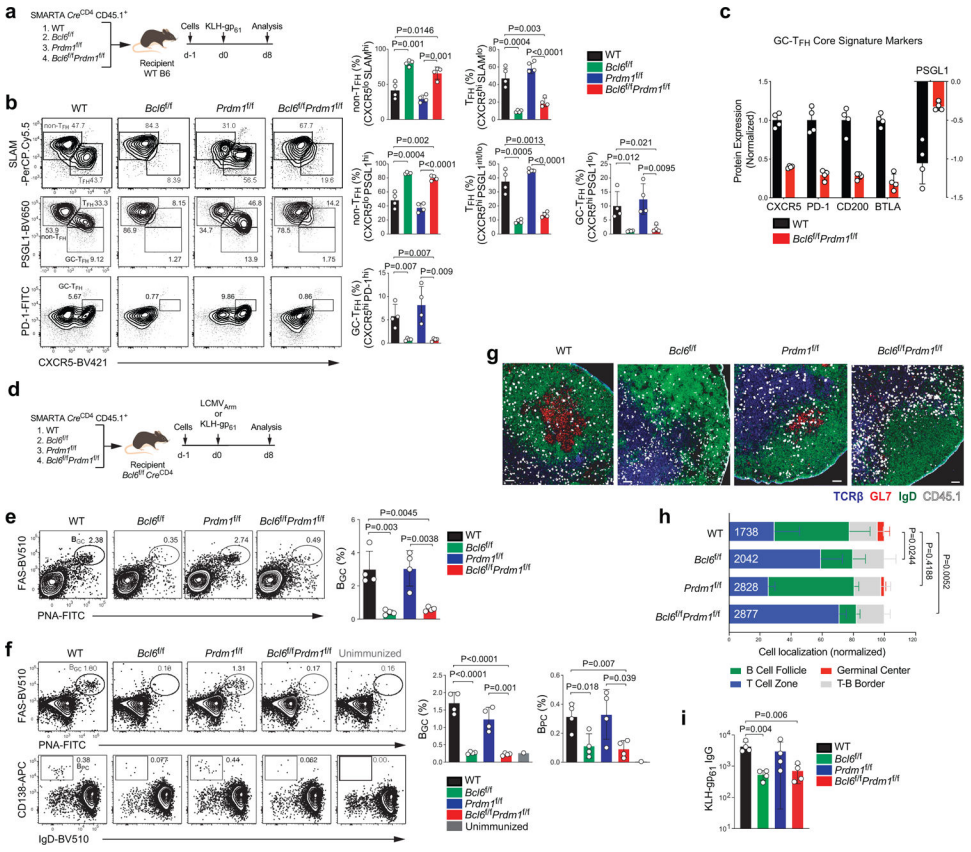

Figure 1. T_{FH} differentiation is not the default pathway.

a, Schematic of the SMARTA cell transfer system used for KLH-gp_{61} immunization. wild-type, *Bcl6*$^{f/f}$, *Prdm1*$^{f/f}$, and *Bcl6*$^{f/f}$*Prdm1*$^{f/f}$ *Cre*^{CD4} SMARTA CD4^{+} T cells were transferred to C57BL/6 host mice, followed by immunization of the host mice with KLH-gp_{61} in alum + cGAMP adjuvant, and analyzed 8 days later. See Fig. 1b and Extended Data Fig.1c–d.

b, Representative flow cytometry of GC-T_{FH}, T_{FH} and non-T_{FH} SMARTA cell subsets from draining LNs (dLNs) of KLH-gp_{61} immunized mice. Three independent experiments were performed; each dot represents one mouse (n = 4). Data are mean ± s.d., unpaired two-tailed Student's t-test.

c, wild-type, *Bcl6*$^{f/f}$, *Prdm1*$^{f/f}$, and *Bcl6*$^{f/f}$*Prdm1*$^{f/f}$ *Cre*^{CD4} SMARTA CD4^{+} T cells were transferred to C57BL/6 host mice, followed by infection of the host mice with $LCMV_{Arm}$, and analyzed 7 days later. Relative protein expression of GC-T_{FH} core signature markers, gated on CXCR5^{+} T_{FH} cells. gMFI value of each gene was normalized to wild-type. Three independent experiments were performed; each dot represents one mouse (n = 4). Data are mean ± s.d., unpaired two-tailed Student's t-test. See Extended Data Fig.1e.

d, Schematic of the SMARTA cell transfer system used for $LCMV_{Arm}$ infection or KLH-gp_{61} immunization. Wild-type, *Bcl6*$^{f/f}$, *Prdm1*$^{f/f}$, and *Bcl6*$^{f/f}$*Prdm1*$^{f/f}$ *Cre*^{CD4} SMARTA CD4^{+} T cells were transferred to *Bcl6*$^{f/f}$*Prdm1*$^{f/f}$ *Cre*^{CD4} host mice, followed by infection or immunization of the host mice with $LCMV_{Arm}$ or KLH-gp_{61} in alum + cGAMP adjuvant, and analyzed 8 days later. See Fig.1e–i and Extended Data Fig.1h–i.

e, Representative flow cytometry gate of B_{GC} cells from spleens of $LCMV_{Arm}$ infected mice. Three independent experiments performed; each dot represents one mouse (n = 4). Data are mean ± s.d., unpaired two-tailed Student's t-test.

f, Representative flow cytometry of B_{GC} cells and B_{PC} from dLNs of KLH-gp_{61} immunized mice. Two independent experiments were performed; each dot represents one mouse (n = 4). Data are mean ± s.d., unpaired two-tailed Student's t-test.

g, Histology of dLNs at d8 after KLH-gp_{61} immunization in Fig.1f. Magnified images from Extended Data Fig.1g are shown. Blue, TCRβ; red, GL7; green, IgD; white, CD45.1 SMARTA. SMARTA cells were presented with large dots for clarity. Scale bar, 200 μm.

h, Quantification of results in Fig. 1i. Total counted number of SMARTA cells were indicated.

i, Serum antigen-specific IgG endpoint titers at d8 after KLH-gp_{61} immunization in Fig.1f. Two independent experiments were performed; each dot represents one mouse (n = 4). Data are mean ± s.d., unpaired two-tailed Student's t-test.

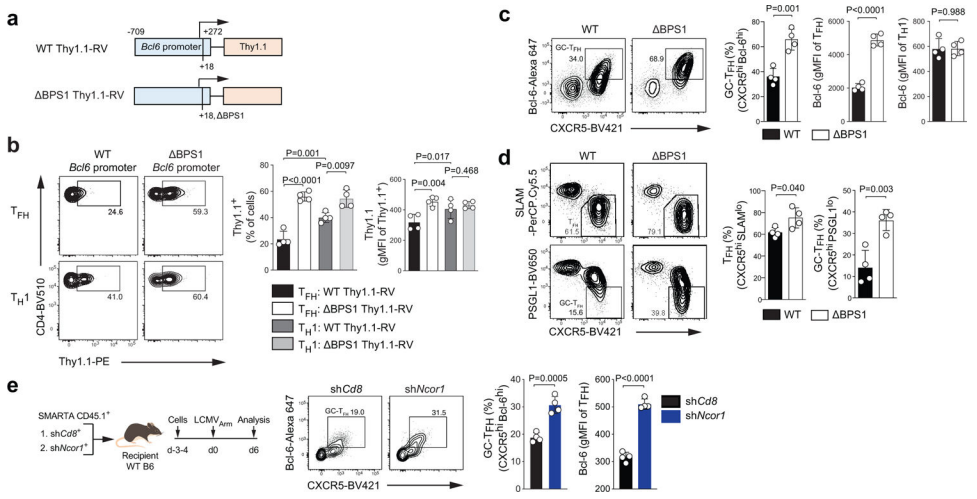

Figure 2. Bcl-6 exhibits direct negative autoregulatory feedback.

a, Schematic diagram of *Bcl6* promoter RV plasmid. Wild-type or ΔBPS1 *Bcl6* promoter Thy1.1-RV were generated based on pQdT SIN vector.

b, Representative flow cytometry and quantification of flow cytometry gate of Thy1.1 reporter positive cells, gated on CXCR5^{+} T_{FH} or CXCR5^{lo} T_H1 cells from spleens of C57BL/6 host mice given SMARTA CD4^{+} T cells transduced with wild-type-RV or ΔBPS1-RV, followed by infection of the host mice with $LCMV_{Arm}$, and analyzed 7 days after infection. Three independent experiments were performed; each dot represents one mouse (n = 4). Data are mean ± s.d., unpaired two-tailed Student's t-test. See Extended Data Fig.2c–d.

c,d, Phenotyping of wild-type and ΔBPS1 SMARTA cells from C57BL/6 host mice given wild-type or ΔBPS1 SMARTA CD4^{+} T cells, followed by infection of the host mice with $LCMV_{Arm}$, and analyzed 7 days after infection. Representative flow cytometry of T_{FH} and GC-T_{FH} SMARTA cell subsets from spleens of $LCMV_{Arm}$ infected mice. Two independent experiments were performed; each dot represents one mouse (n = 4). Data are mean ± s.d., unpaired two-tailed Student's t-test. See Extended Data Fig.2 for experimental scheme (g) and quantification of gene expression level (h).

e, SMARTA CD4^{+} T cells transduced with sh*Cd8*-RV or sh*Ncor1*-RV were transferred to C57BL/6 host mice, followed by infection of the host mice with $LCMV_{Arm}$, and analyzed 7 days after infection. Representative flow cytometry of GC-T_{FH} RV^{+} SMARTA cell subsets from spleens of $LCMV_{Arm}$ infected mice. Two independent experiments were performed; each dot represents one mouse (n = 4). Data are mean ± s.d., unpaired two-tailed Student's t-test.

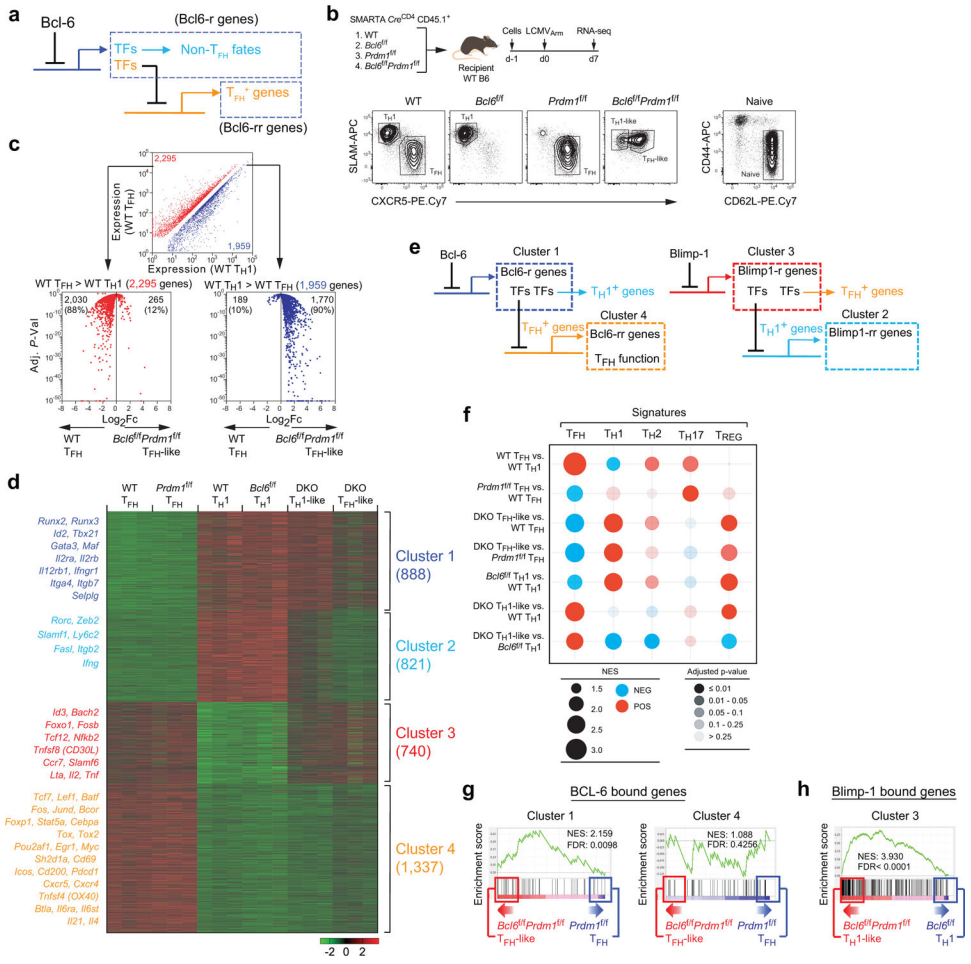

Figure 3. A testable simple circuitry model of T_{FH} differentiation.

a, A hypothetical model of Bcl-6 on the regulation of non-T_{FH} and T_{FH} genes. Bcl6-r, genes repressed by Bcl-6. Bcl6-rr, genes repressed by repressors that are repressed by Bcl-6.

b, Schematic of the SMARTA cell transfer system used for RNA-seq analysis. T_H1 ($CXCR5^{lo}SLAM^{hi}$) populations from wild-type and *Bcl6*$^{f/f}$ Cre^{CD4} SMARTA cells, T_{FH} ($CXCR5^{hi}SLAM^{lo}$) populations from wild-type and *Prdm1*$^{f/f}$ Cre^{CD4} SMARTA cells, T_H1-like ($CXCR5^{lo}SLAM^{int}$) and T_{FH}-like ($CXCR5^{+}SLAM^{int}$) populations from *Bcl6*$^{f/f}$*Prdm1*$^{f/f}$ Cre^{CD4} SMARTA cells were sorted from spleens of C57BL/6 host mice given wild-type, *Bcl6*$^{f/f}$, *Prdm1*$^{f/f}$, and *Bcl6*$^{f/f}$*Prdm1*$^{f/f}$ Cre^{CD4} SMARTA $CD4^{+}$ T cells, followed by infection of the host mice with $LCMV_{Arm}$, and analyzed 7 days later. Naive SMARTA cells were isolated as $CD44^{lo}CD62L^{hi}CD45.1^{+}$ from uninfected mice. Representative flow cytometry of T_{FH}, T_H1, T_{FH}-like, and T_H1-like subsets from three independent experiments.

c, Upper, scatter plot of genes upregulated (red) or downregulated (blue) in T_{FH} cells relative to their expression in T_H1 cells (1.4-fold cut off, Adj. P <0.05). Lower, volcano plots of gene expression changes between wild-type T_{FH} cells and *Bcl6*$^{f/f}$*Prdm1*$^{f/f}$ T_{FH}-like cells (horizontal axis) against Adj. *P*-value (vertical axis). Numbers indicate total and percent of those genes upregulated in wild-type T_{FH} cells (top left) or *Bcl6*$^{f/f}$*Prdm1*$^{f/f}$ T_{FH}-like cells (top right). T_H1 cell-associated genes, upregulated in wild-type T_H1 cells versus wild-type T_{FH} cells (WT T_H1 > WT T_{FH}); T_{FH} cell-associated genes, upregulated in wild-type T_{FH}

cells versus wild-type T_H1 cells (WT T_{FH} > WT T_H1). Adj. *P*-values for multiple test correction were determined using Benjamini-Hochberg algorithm.

d, Gene expression changes were clustered by MAP-DP analysis. Scale, row z-score. DKO, *Bcl6*$^{f/f}$*Prdm1*$^{f/f}$ *Cre*^{CD4}.

e, Left, a hypothetical model of Bcl-6 regulation of Bcl6-rr T_{FH}^+ genes in Cluster 4 by inhibition of Bcl6-r TFs in Cluster 1. Right, a hypothetical model of Blimp-1 regulation of Blimp-1-rr T_H1^+ genes in Cluster 2 by inhibition of Blimp-1-r TFs in Cluster 3.

f, Multiple gene set enrichment analyses (GSEA) for identifying and comparing gene signatures in $CD4^+$ T cells between subpopulations. Blue indicates a negative association, and red indicates a positive association. Circle size is proportional to NES (scale: 1.5–3.0). Tint indicates adjusted *P*-value that were corrected using Benjamini-Hochberg algorithm.

g, GSEA of BCL-6 bound genes from human tonsillar GC-T_{FH}[24] compared to Cluster 1 genes (left) or Cluster 4 genes (right) differentially expressed between *Bcl6*$^{f/f}$*Prdm1*$^{f/f}$ T_{FH}-like cells and *Prdm1*$^{f/f}$ T_{FH} cells. The ticks below the line correspond to the rank of each gene that is defined by p-value of gene expression change between *Bcl6*$^{f/f}$*Prdm1*$^{f/f}$ T_{FH}-like and *Prdm1*$^{f/f}$ T_{FH}. NES, normalized enrichment score; FDR, false discovery rate.

h, GSEA of Blimp-1 bound genes from activated CD8 T cells[54] in comparison of Cluster 3 genes differentially expressed between *Bcl6*$^{f/f}$*Prdm1*$^{f/f}$ T_H1-like cells and *Bcl6*$^{f/f}$ T_H1 cells.

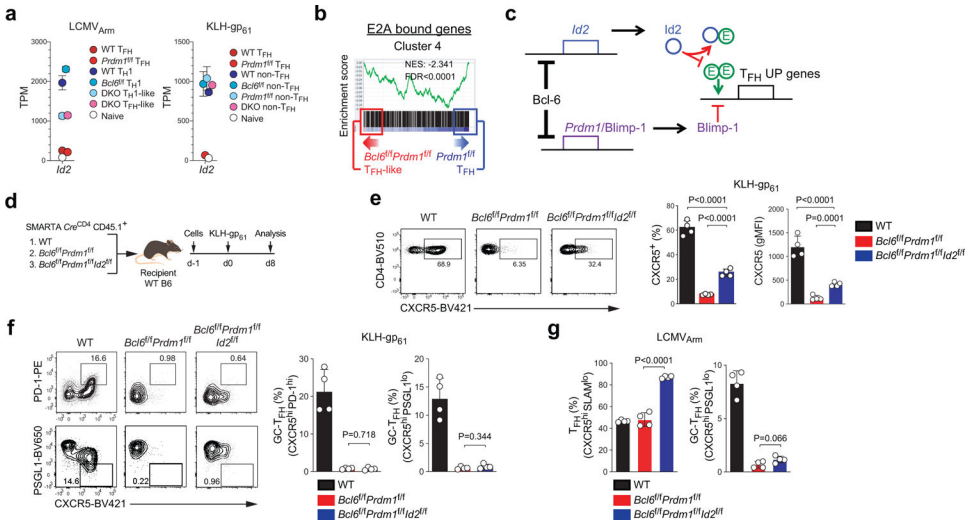

Figure 4. Bcl-6 drives CXCR5 expression via repression of Id2-E2A pathway

a, Gene expression of *Id2* from RNA-seq data of $LCMV_{Arm}$ infected mice or KLH-gp_{61} immunized mice. Each data point was collected from three ($LCMV_{Arm}$) or four (KLH-gp_{61}) independent experiments.

b, GSEA of E2A bound genes from thymocytes[22,55] in comparison to Cluster 4 genes between *Bcl6*$^{f/f}$*Prdm1*$^{f/f}$ T_{FH}-like cells and *Prdm1*$^{f/f}$ T_{FH} cells.

c, A hypothetical model of Bcl-6 regulation of T_{FH} genes primarily via inhibition of Id2 and *Prdm1*/Blimp-1.

d, Schematic of the SMARTA cell transfer system used for KLH-gp_{61} immunization. Wild-type, *Bcl6*$^{f/f}$*Prdm1*$^{f/f}$, or *Bcl6*$^{f/f}$*Prdm1*$^{f/f}$*Id2*$^{f/f}$ *Cre*^{CD4} SMARTA $CD4^+$ T were transferred to C57BL/6 host mice, followed by immunization of the host mice with KLH-gp_{61} in alum + cGAMP, and analyzed 8 days later. See Fig. 4e,f and Extended Data Fig.4a.

e,f, Representative flow cytometry of $CXCR5^{hi}$ T_{FH}, $CXCR5^{hi}PD\text{-}1^{hi}$ and $CXCR5^{hi}PSGL1^{lo}$ GC-T_{FH} SMARTA cell subsets from dLNs of KLH-gp_{61} immunized mice in Fig.4d. Two independent experiments were performed; each dot represents one mouse (n = 4). Data are mean ± s.d., unpaired two-tailed Student's t-test.

g, Quantification of $CXCR5^{hi}SLAM^{lo}$ T_{FH} and $CXCR5^{hi}PSGL1^{lo}$ GC-T_{FH} cells, gated on SMARTA cells from spleens of $LCMV_{Arm}$ infected mice. Two independent experiments were performed; each dot represents one mouse (n = 4). Data are mean ± s.d., unpaired two-tailed Student's t-test. See Extended Data Fig.4b–g.

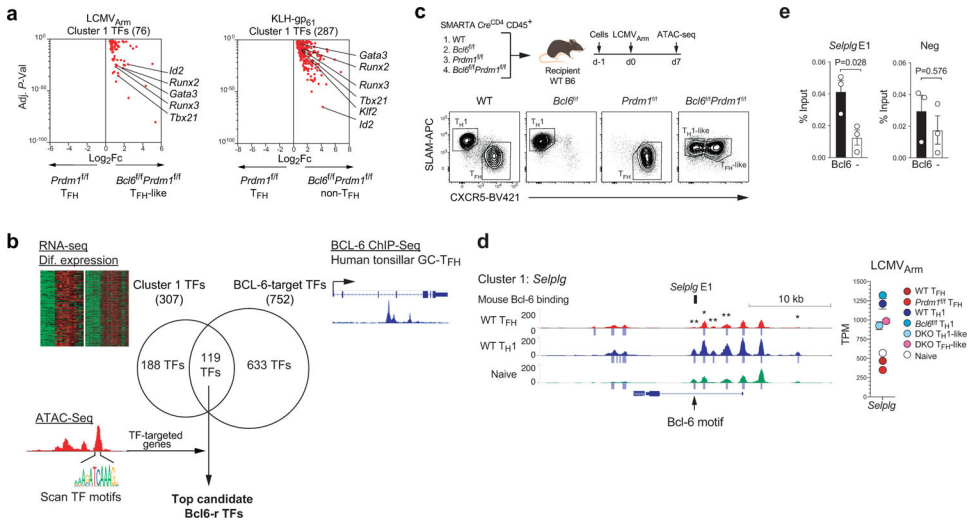

Figure 5. Integrated analysis of multiple genetic backgrounds and data types.

a, Volcano plot of gene expression changes of Cluster 1 TFs between *Bcl6*$^{f/f}$*Prdm1*$^{f/f}$ T_{FH}-like cells and *Prdm1*$^{f/f}$ T_{FH} cells (LCMV$_{Arm}$ infection) or between *Bcl6*$^{f/f}$*Prdm1*$^{f/f}$ non-T_{FH} cells and *Prdm1*$^{f/f}$ T_{FH} cells (KLH-gp$_{61}$ immunization) (1.4-fold cut off, Adj. P<0.05); 76 TFs from LCMV$_{Arm}$ infection; 287 TFs from KLH-gp$_{61}$ immunization; combined 307 TF). Adj. P-values for multiple test correction were determined using Benjamini-Hochberg algorithm. Each data point was collected from independent experiments. Select genes of interest are labeled.

b, Schematic of the integrated analytical approach. The composite RNA-seq data with both BCL-6 ChIP-seq data from human tonsillar GC-T_{FH} cells and ATAC-seq of T_{FH} and T_H1 cells from wild-type, *Bcl6*$^{f/f}$, *Prdm1*$^{f/f}$ and *Bcl6*$^{f/f}$*Prdm1*$^{f/f}$ *Cre*^{CD4} SMARTA cells. Among the Cluster 1 TFs in Fig.5a, 119 TFs represented BCL-6-bound gene loci in human GC-T_{FH} cells. ATAC-seq and TF motifs scanning filters top Bcl6-r TF candidates.

c, Schematic of the experimental plan to generate ATAC-seq data. T_H1 (CXCR5^{lo}SLAM^{hi}) populations from wild-type and *Bcl6*$^{f/f}$ Cre^{CD4} SMARTA cells, T_{FH} (CXCR5^{hi}SLAM^{lo}) populations from wild-type and *Prdm1*$^{f/f}$ Cre^{CD4} SMARTA cells, T_H1-like (CXCR5^{lo}SLAM^{int}) and T_{FH}-like (CXCR5^{+}SLAM^{int}) populations from *Bcl6*$^{f/f}$*Prdm1*$^{f/f}$ Cre^{CD4} SMARTA cells were sorted from spleens of C57BL/6 host mice given wild-type, *Bcl6*$^{f/f}$, *Prdm1*$^{f/f}$, and *Bcl6*$^{f/f}$*Prdm1*$^{f/f}$ Cre^{CD4} SMARTA cells, followed by infection of the host mice with LCMV$_{Arm}$, and analyzed 7 days later. Naive SMARTA cells were isolated as CD44^{lo}CD62L^{hi}CD45.1^{+} from uninfected mice. Representative flow cytometry of T_{FH}, T_H1, T_{FH}-like, and T_H1-like subsets from three independent experiments.

d, Genome-browser tracks depict ATAC-seq chromatin accessibility and TF occupancy. Peak calls indicated below each track. A Bcl-6 liftover peak from human to mouse reference genome is indicated. * and ** indicate DEseq2 raw P-val ≤ 0.05 and ≤ 0.01, respectively, in comparison between wild-type T_{FH} and T_H1. Gene expression from RNA-seq data of LCMV$_{Arm}$ infected mice is graphed. Each data point was collected from three independent experiments. DKO, *Bcl6*$^{f/f}$*Prdm1*$^{f/f}$ *Cre*^{CD4}.

e, ChIP-qPCR analysis of Bcl-6 at *Selplg* E1 or negative control region among chromatin prepared from CXCR5^{hi} T_{FH} cells from spleens of C57BL/6 host mice given SMARTA

$CD4^+$ T cells transduced with myctagN-*Bcl6*-RV, followed by infection of the host mice with $LCMV_{Arm}$, and analyzed 7 days after infection. ChIP was performed using an anti-myc IgG or control IgG. Three independent experiments were performed. Each data point is from an independent experiment (n=3) and presented as a percent of input. Data are mean ± s.e.m., unpaired two-tailed Student's t-test.

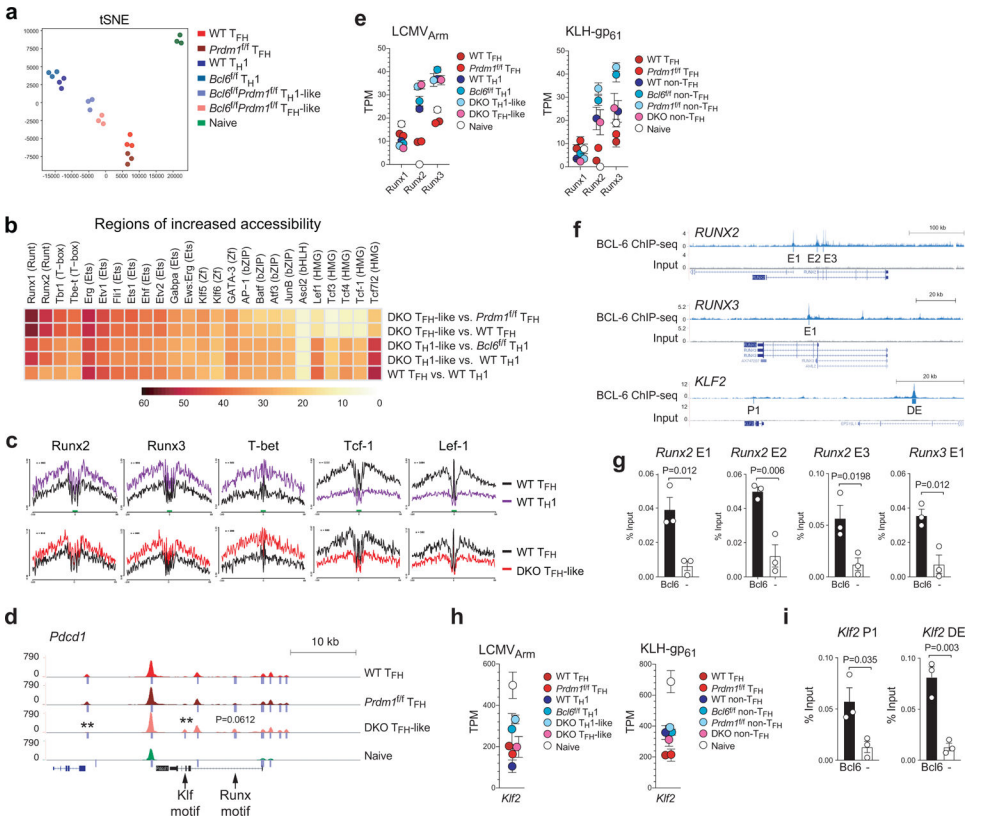

Figure 6. Identification of candidate TFs

a, tSNE analysis of ATAC-seq chromatin accessibility.

b, Heatmap plots representing the frequencies of the most enriched TF motifs in regions of increased accessibility (relatively more open in first group than second group, DEseq2 raw *P*-val < 0.05). Scale, motif frequencies (%).

c, TF footprints derived from ATAC-seq reads over representative TF motifs within accessible ATAC-seq regions.

d, Genome-browser tracks depict ATAC-seq chromatin accessibility and TF occupancy. Peak calls indicated below each track. ** indicates DEseq2 raw p-val ≤ 0.01 in comparison between *Bcl6*$^{f/f}$*Prdm1*$^{f/f}$ Cre^{CD4} T_{FH}-like and *Prdm1*$^{f/f}$ Cre^{CD4} T_{FH}.

e, Gene expression of Runx1, Runx2, and Runx3 from RNA-seq data of $LCMV_{Arm}$ infected mice or KLH-gp_{61} immunized mice. Each data point was collected from three ($LCMV_{Arm}$) or four (KLH-gp_{61}) independent experiments.

f, Genome-browser tracks depict BCL-6 ChIP-Seq peaks at *RUNX2*, *RUNX3*, and *KLF2* loci. Peak calls indicated below each track.

g,i. ChIP-qPCR analysis of Bcl-6 at *Runx2* E1, E2 and E3, *Runx3* E1, or *Klf2* P1 and DE among chromatin prepared from CXCR5^{hi} T_{FH} cells as shown in Fig.5e. Three independent experiments were performed. Each data point is from an independent experiment (n=3) and presented as a percent of input. Data are mean ± s.e.m., unpaired two-tailed Student's t-test.

h, Gene expression of *Klf2* from RNA-seq data of $LCMV_{Arm}$ infected mice or KLH-gp_{61} immunized mice. Each data point was collected from three ($LCMV_{Arm}$) or four (KLH-gp_{61}) independent experiments.

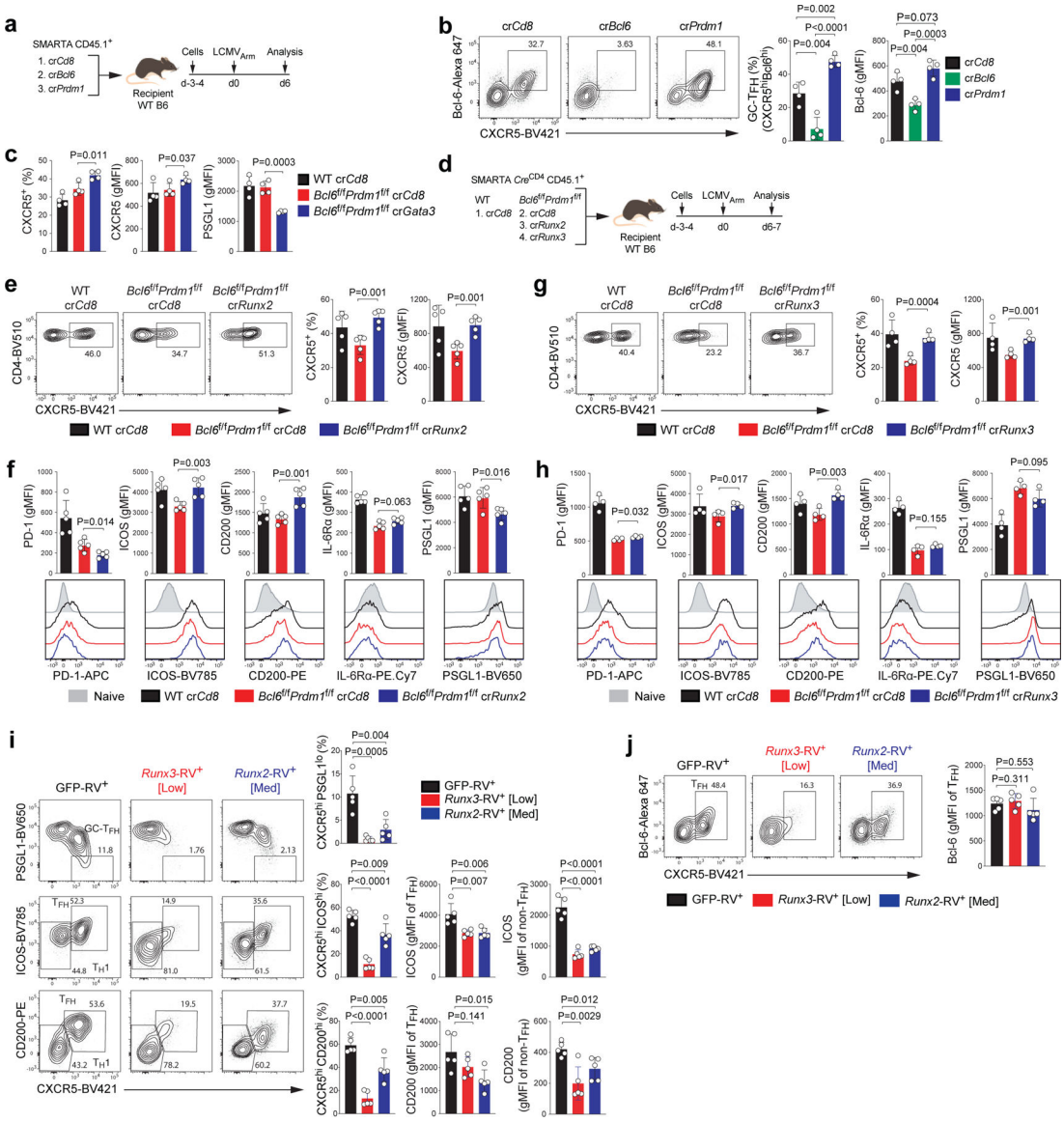

Figure 7. Identification of Runx2, Runx3, and GATA-3 as repressors of T_{FH} genes, acting downstream of Bcl-6.

a, Schematic of the CRISPR/Cas9-mediated gene knockdown of SMARTA cell system used for testing *Bcl6* and *Prdm1* in $LCMV_{Arm}$ infection. SMARTA $CD4^+$ T cells transfected with cr*Cd8*, cr*Bcl6*, or cr*Prdm1* were transferred to C57BL/6 host mice, followed by infection of the host mice with $LCMV_{Arm}$, and analyzed 6 days later.

b, Representative flow cytometry of GC-T_{FH} SMARTA cell subsets from spleens of $LCMV_{Arm}$ infected mice in a. Two independent experiments were performed; each dot represents one mouse (n = 4). Data are mean ± s.d., unpaired two-tailed Student's t-test.

c, Quantification of results from cr*Cd8*$^+$ and cr*Gata3*$^+$ SMARTA cells from spleens of $LCMV_{Arm}$ infected mice. Three independent experiments were performed; each dot represents one mouse (n = 4). Data are mean ± s.d., unpaired two-tailed Student's t-test. See Extended Data Fig.7h,i,l,m.

d, Schematic of the CRISPR/Cas9-mediated gene knockdown of SMARTA cell system used for testing *Runx2* and *Runx3* in $LCMV_{Arm}$ infection. wild-type or $Bcl6^{f/f}Prdm1^{f/f}$ Cre^{CD4} SMARTA $CD4^+$ T cells transfected with cr*Cd8*, cr*Runx2*, or cr*Runx3* were transferred to C57BL/6 host mice, followed by infection of the host mice with $LCMV_{Arm}$, and analyzed 6–7 days later. See e–h and Extended Data Fig.7j–k.

e,g, Representative flow cytometry of T_{FH} SMARTA cell subsets from spleens of $LCMV_{Arm}$ infected mice in d. Three independent experiments were performed; each dot represents one mouse (e, n = 5;g, n = 4). Data are mean ± s.d., unpaired two-tailed Student's t-test.

f,h, Quantification of GC-T_{FH} core signature markers, gated on SMARTA cells in d. $CD44^{lo}$ naive $CD4^+$ T cells were used as a negative control.

i,j, Representative flow cytometry of T_H1, T_{FH} and GC-T_{FH} RV^+ SMARTA cell subsets from spleens of C57BL/6 host mice given SMARTA $CD4^+$ T cells transduced with pMIG (GFP-RV^+), pMIG-Runx3myc (*Runx3*-RV^+ [Low]), or pMIG-Runx2myc (*Runx2*-RV^+ [Med]), followed by infection of the host mice with $LCMV_{Arm}$, and analyzed 7 days after infection. Two independent experiments were performed; each dot represents one mouse (n = 5). Data are mean ± s.d., unpaired two-tailed Student's t-test.

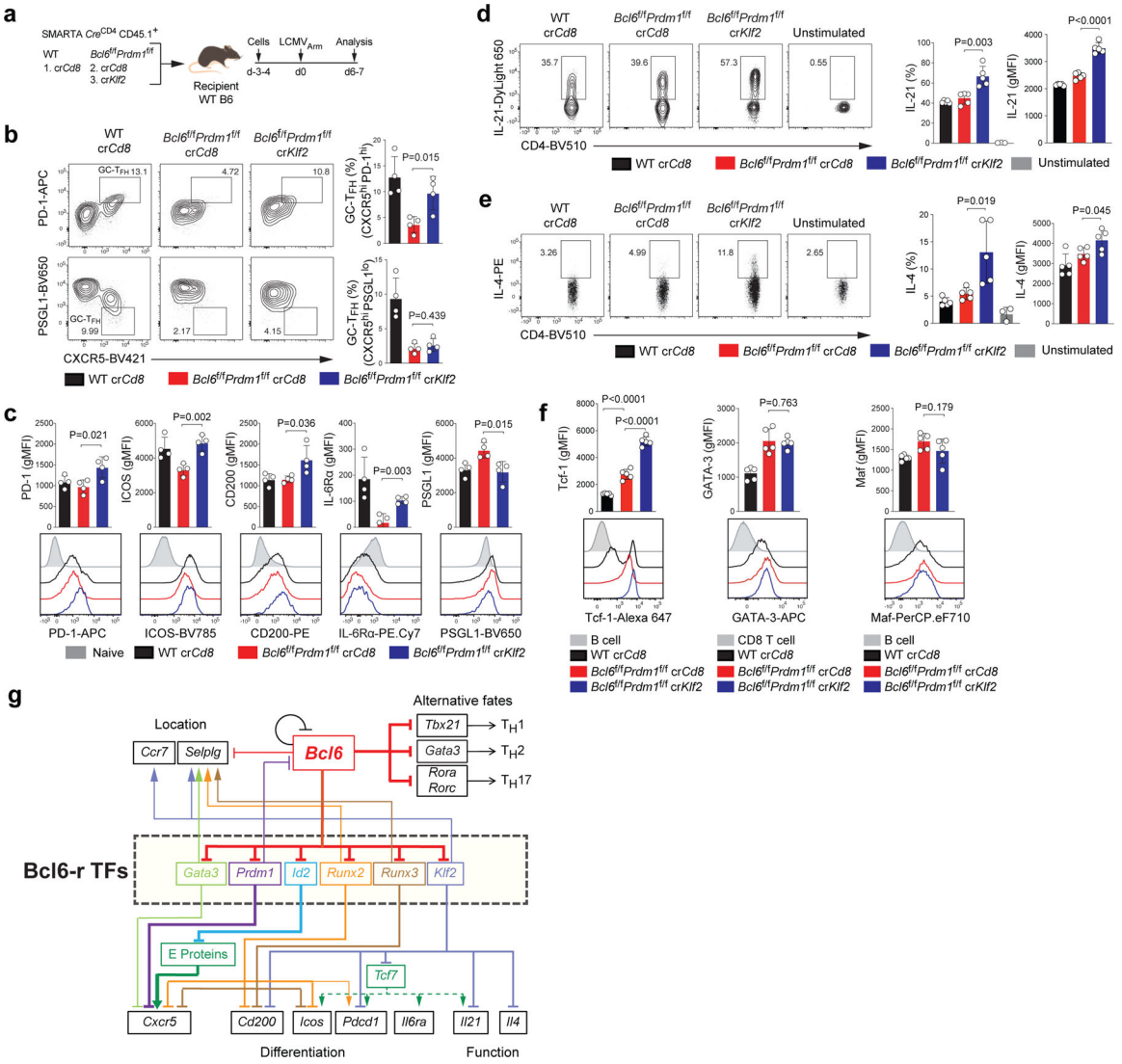

Figure 8. Identification of Klf2 as a repressor acting downstream of Bcl-6 regulating major T_{FH} genes.

a, Schematic of the CRISPR/Cas9-mediated gene knockdown of SMARTA cell system used for testing *Klf2* in $LCMV_{Arm}$ infection. wild-type or $Bcl6^{f/f}Prdm1^{f/f}$ Cre^{CD4} SMARTA $CD4^+$ T cells transfected with cr*Cd8* or cr*Klf2* were transferred to C57BL/6 host mice, followed by infection of the host mice with $LCMV_{Arm}$, and analyzed 6–7 days later. See Fig.8b–c and Extended Data Fig.9a,b.

b, Representative flow cytometry of T_{FH} and GC-T_{FH} cells, gated on SMARTA cells from spleens of $LCMV_{Arm}$ infected mice in a. Three independent experiments were performed; each dot represents one mouse (n = 4). Data are mean ± s.d., unpaired two-tailed Student's t-test.

c, Quantification of GC-T_{FH} core signature markers, gated on SMARTA cells from spleens of $LCMV_{Arm}$ infected mice in a. $CD44^{lo}$ naive $CD4^+$ T cells were used as a negative control.

d,e, wild-type or *Bcl6*$^{f/f}$*Prdm1*$^{f/f}$ *Cre*^{CD4} SMARTA CD4^{+} T cells transfected with cr*Cd8* or cr*Klf2* were transferred to C57BL/6 host mice, followed by immunization of the host mice with KLH-gp$_{61}$ and alum + cGAMP, and analyzed 8 days later. Representative flow cytometry and quantification of gp$_{66}$-restimulated IL-21^{+} and IL-4^{+} SMARTA cells from dLNs of KLH-gp$_{61}$ immunized mice. Two independent experiments were performed; each dot represents one mouse (n = 5). Data are mean ± s.d., unpaired two-tailed Student's t-test. See Extended Data Fig.9d for experimental design.

f, Quantification of expression of Tcf-1, GATA-3, and Maf, gated on SMARTA cells from dLNs of KLH-gp$_{61}$ immunized mice in Extended Data Fig.9d.

g, A circuitry model of the regulation of T$_{FH}$ genes upregulated by Bcl-6 through repression of repressor TFs.